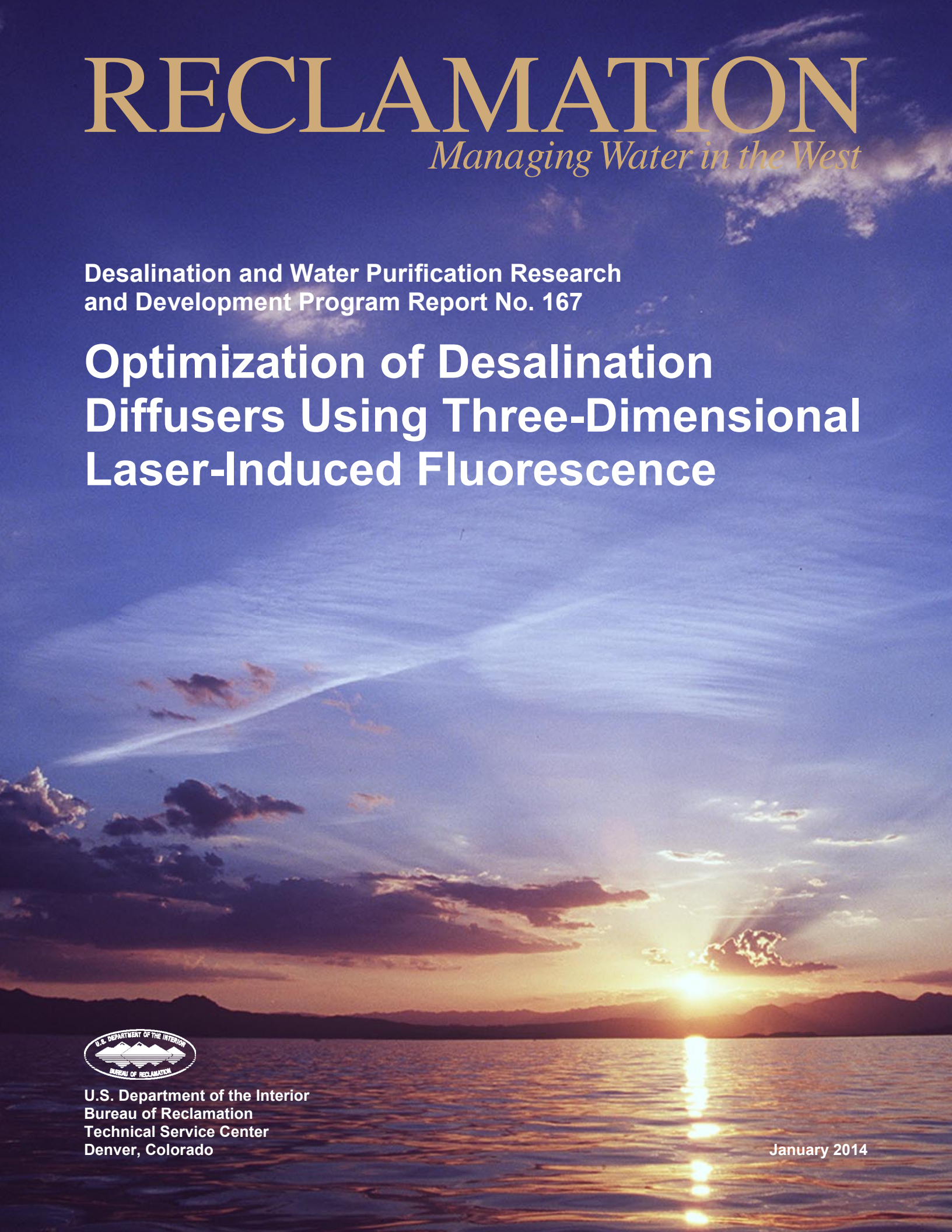

RECLAMATION

Managing Water in the West

Desalination and Water Purification Research and Development Program Report No. 167

Optimization of Desalination Diffusers Using Three-Dimensional Laser-Induced Fluorescence

U.S. Department of the Interior
Bureau of Reclamation
Technical Service Center
Denver, Colorado

January 2014

REPORT DOCUMENTATION PAGE			Form Approved OMB No. 0704-0188

1. REPORT DATE *(DD-MM-YYYY)*	2. REPORT TYPE	3. DATES COVERED *(From - To)*
01-2014	Final	2011-2014

4. TITLE AND SUBTITLE	5a. CONTRACT NUMBER
Optimization of Desalination Diffusers Using Three-Dimensional Laser-Induced Fluorescence	Agreement No. R11 AC81 535
	5b. GRANT NUMBER
	5c. PROGRAM ELEMENT NUMBER
6. AUTHOR(S) Philip J. W. Roberts and Ozeair Abessi	5d. PROJECT NUMBER
	5e. TASK NUMBER
	5f. WORK UNIT NUMBER

7. PERFORMING ORGANIZATION NAME(S) AND ADDRESS(ES)	8. PERFORMING ORGANIZATION REPORT NUMBER
School of Civil and Environmental Engineering Georgia Institute of Technology Atlanta, Georgia 30332	
9. SPONSORING/MONITORING AGENCY NAME(S) AND ADDRESS(ES)	10. SPONSOR/MONITOR'S ACRONYM(S)
Bureau of Reclamation U.S. Department of the Interior Denver Federal Center PO Box 25007, Denver, CO 80225-0007	Reclamation
	11. SPONSOR/MONITOR'S REPORT NUMBER(S) DWPR Report No. 167

12. DISTRIBUTION/AVAILABILITY STATEMENT
Available from the National Technical Information Service,
Operations Division, 5285 Port Royal Road, Springfield VA 22161

13. SUPPLEMENTARY NOTES
Online at https://www.usbr.gov/research/dwpr/DWPR_Reports.html

14. ABSTRACT
The results of extensive measurements on model studies of multiport diffusers discharging brine concentrate are reported. A three-dimensional laser-induced fluorescence (3DLIF) system was used to map tracer concentration profiles in the various flows. A wide range of parameters, typical of those expected in actual ocean outfall diffusers, was tested. In this report, the experimental techniques, procedures, and results are presented.

15. SUBJECT TERMS
Desalination, diffusers, jets , currents, ocean outfall diffusers

16. SECURITY CLASSIFICATION OF:			17. LIMITATION OF ABSTRACT	18. NUMBER OF PAGES	19a. NAME OF RESPONSIBLE PERSON
a. REPORT	b. ABSTRACT	THIS PAGE			John Walp
U	U	U			19b. TELEPHONE NUMBER *(Include area code)* 303-445-2871

Desalination and Water Purification Research and Development Program Report No. 167

Optimization of Desalination Diffusers Using Three-Dimensional Laser-Induced Fluorescence

Prepared for the Bureau of Reclamation Under Agreement No. R11 AC81 535

by

Philip J. W. Roberts
and
Ozeair Abessi

School of Civil and Environmental Engineering
Georgia Institute of Technology
Atlanta, Georgia 30332

U.S. Department of the Interior
Bureau of Reclamation
Technical Service Center
Denver, Colorado

January 2014

MISSION STATEMENTS

The U.S. Department of the Interior protects America's natural resources and heritage, honors our cultures and tribal communities, and supplies the energy to power our future.

The mission of the Bureau of Reclamation is to manage, develop, and protect water and related resources in an environmentally and economically sound manner in the interest of the American public.

Disclaimer

The views, analysis, recommendations, and conclusions in this report are those of the authors and do not represent official or unofficial policies or opinions of the United States Government, and the United States takes no position with regard to any findings, conclusions, or recommendations made. As such, mention of trade names or commercial products does not constitute their endorsement by the United States Government.

CONTENTS

LIST OF FIGURES

LIST OF FIGURES (continued)

LIST OF FIGURES (continued)

LIST OF TABLES

SUMMARY

The results of extensive measurements on model studies of multiport diffusers discharging brine concentrate are reported. A three-dimensional laser-induced fluorescence (3DLIF) system was used to map tracer concentration profiles in the various flows. A wide range of parameters, typical of those expected in actual ocean outfall diffusers, was tested. In this report, the experimental techniques, procedures, and results are presented.

A dimensional analysis of the main variables is first presented to aid in the analysis of the data, to aid in interpretation of the experimental results, and to present the essential results in the most efficient manner. Analyses are presented for stationary single jets, multiple jets, and flowing currents. Particular emphasis was placed on the major flow properties and those of most importance in prediction of environmental impact and diffuser design: the rise height, lower boundary impact point, dilutions at the terminal rise height, impact point and end of the near field, and the length of the near field.

The experimental procedures and instrumentation are then described. The experiments were performed in a specially designed glass-walled flume in the Environmental Fluid Mechanics laboratory at the School of Civil Engineering at Georgia Tech.

The experimental results are then presented.

The first series of experiments were for multiport diffusers with discharges from one or both sides in stationary environments. It was found that the results did not follow the asymptotic slot jet results expected for closely spaced jets. The dilutions were more sensitive to port spacing and lower than expected and the rise heights decreased as port spacing decreased. The reason was found to be that the jets had an initial transient behavior where the rise height was initially high, then decreased as the descending flow was re-entrained by the rising flow. Entraining flow could not penetrate to the inner core, reducing dilution and rise height. Dilutions with diffusers discharging to both or one side were not significantly different. To ensure adequate supply of diluting entrained flow, it is recommended that the ports are spaced such that $s/d\mathsf{F} > 2$.

Multiport diffusers in currents flowing perpendicular to the diffuser axis were then addressed. Diffusers discharging to one side were first studied for co-flowing (current direction the same as the jets) and counter-flowing (current direction opposed to the jets) cases. The results were presented as normalized rise height, jet trajectories, and dilutions as functions of a dimensionless current speed parameter. Dilutions generally increased with current speed and depended on port spacing. For counter-flowing currents, a critical condition occurred at $u_r\mathsf{F} \approx 0.67$ where the jet was deflected back onto itself.

Multiport diffusers discharging from both sides into flowing currents were conducted for two cases: The diffuser pipe was located on the channel bottom (referred to as the blocked case), and the pipe was elevated above the bottom (the unblocked case) with a gap to allow flow to pass beneath the diffuser. It was found that the flow can be significantly affected by the presence or absence of the gap.

These results imply that care is needed in diffuser design to ensure that diluting water is freely available and unimpeded, and entrainment-type mathematical models should be used with caution in cases where it is not freely available.

Rosette diffusers were then investigated as these are often now being used for brine disposal (for example, Sydney, Australia). The model rosettes consisted of risers each with four ports. Diffusers with one or three risers were studied and the effective riser spacing was varied. Two configurations with different rotations of the risers about their vertical axes were tested.

Single risers with no current were first tested. The riser rotation had negligible effect on dilution or location of the near field. The near field dilution was affected by riser spacing for $s/d\mathsf{F} < \approx 2.5$, but not for wider spacings. Rosette risers resulted in slightly lower dilutions than comparable conventional multiport diffusers for wide port spacings but were similar for narrower spacings.

Rosettes in flowing currents were then tested. The effect of riser rotation was again found to be insignificant. Complex merging patterns were observed as discussed in the report. Quantitative results are presented in dimensionless form to aid in the design of multiport rosette diffusers.

Experiments were then conducted on single jets of various nozzle angles in stationary environments. The results were compared with two well-known mathematical models: CORMIX and UM_3 of Visual Plumes. It was found that the dilution was not sensitive to nozzle angle over the range of about 40° to 70°. The mathematical models generally underestimated dilution.

The final set of experiments were to investigate the effect of water depth on jet mixing and dynamics. Tests were performed for nozzle angles of 30°, 45°, and 60° in water depths ranging from very deep to very shallow, in which case the jets impacted the water surface. Three flow regimes were delineated: Deep, transition shallow, and shallow water. For deep water, the top of the jet was well below the water surface and the water depth had no effect. For transition shallow, the top of the jet impacted the water surface, and for shallow water the jet centerline impacted the water surface. Dilutions generally decreased as the water depth became more limited.

A great many experiments, several hundred, were conducted in this study. Each experiment generated several GB of instantaneous and time-averaged tracer concentration data. The data are available for testing and validation of mathematical models of the entrainment type and CFD (Computational Fluid Dynamics).

1. INTRODUCTION

1.1 Objectives

The objective of this study was to improve and optimize the designs of multiport brine concentrate diffusers and improve the predictions of dilution and environmental impact under realistic oceanic conditions. This was achieved by measuring and mapping tracer concentration profiles in the jets and the spreading bottom layer by an innovative three- dimensional Laser-Induced Fluorescence (3DLIF) system that we have developed. Multiport diffusers with the ports arranged conventionally and in "rosette" configurations will be tested as these are the most common designs in practice.

The number of ports, port and riser spacing, and other parameters were systematically varied. The behavior of these discharges under realistic ocean current conditions were then tested. The results at the end of the investigation will be detailed data on the three-dimensional concentration distributions. In addition to this information of a fundamental nature into the hydrodynamics of jet mixing, the results will be used to improve the predictive reliability of mathematical models such as CORMIX. Through the similitude equations, the measured dilutions are applicable to discharges of any concentrate solutions typical of desalination brines.

1.2 Outline

In Section 2 we present a dimensional analysis for the main variables in order to aid in the analysis and for efficient presentation and interpretation of the extensive experimental data that were gathered. First we analyze single jets in stationary environments, then multiple jets from multiport diffusers, then the effects of currents. The effects of shallow water are analyzed in Section 4.8.

The experimental procedures and methods of data reduction are presented in Section 3. The experimental results are presented in Section 4. Multiport diffusers, first in stationary water and then in perpendicular flowing currents are studied. The multiport diffusers can have discharges from one side or both sides. If one-sided, both co-flowing and counter-flowing currents are considered. For discharges from both sides, the direction is immaterial. Rosette diffusers consisting of risers each with four ports are then considered as many brine diffusers are now being constructed in this configuration. Diffusers consisting of either one or three risers are studied first in stationary currents and the effective riser spacing varied. Then rosette diffusers in flowing currents are investigated. Finally, two topics related to single jets are investigated. First, the effect of nozzle orientation on jet dynamics and then the effects of restricted water depth (shallow water) on jets of various nozzle angles. Experimental parameters and results are summarized in Appendix A.

2. ANALYSIS

2.1 Stationary Multiport

2.1.1 Single jet

The main flow characteristics for a single dense jet in a stationary environment are shown in Figure 1. The negative buoyancy of the jet causes it to reach a terminal rise height and then fall back to the lower boundary where it spreads as a density current. Vertical jets fall back onto themselves when discharged into a stationary environment, resulting in lowered dilutions, so inclined jets are more commonly used. A 60° nozzle inclination seems to have been adopted as the de facto standard for diffuser designs.

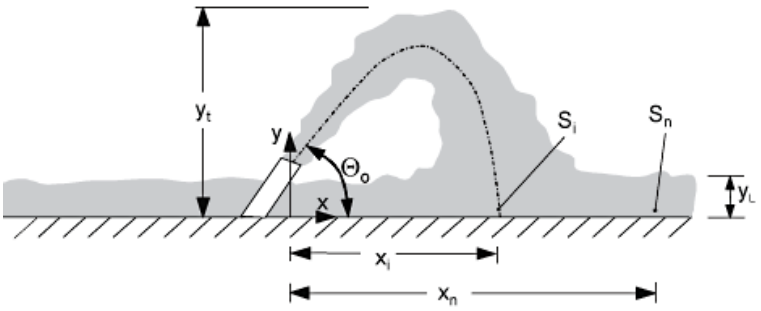

Figure 1. Definition diagram for single dense jet (after Roberts et al., 1997)

The analysis of this case is well known, e.g., Roberts et al. (1997). The jet is primarily characterized by its kinematic fluxes of volume, Q, momentum, M, and buoyancy, B,

$$Q = \frac{\pi}{4} d^2 u; \quad M = uQ; \quad B = g'_o Q \qquad (1)$$

where d is the port diameter, u the jet exit velocity, $g'_o = g(\rho_a - \rho_o)/\rho_o$, is the modified acceleration due to gravity, g the acceleration due to gravity, ρ_a the ambient density and ρ_o the effluent density ($\rho_a > \rho_o$).

As discussed in Roberts et al. and elsewhere, the most important length-scale of the flow is $l_M = M^{3/4}/B^{1/2}$ although this is essentially equal to and more commonly expressed as $d\mathsf{F}$ where F is the jet densimetric Froude number:

$$\mathsf{F} = \frac{u}{\sqrt{g'_o d}} \qquad (2)$$

If the Froude number is greater than about 20, the volume flux, Q, is not dynamically significant (or, equivalently, the nozzle diameter is not a relevant length-scale), Roberts et al. (1997). In that case, any dependent variable, such as the terminal rise height, y_t, is a function of M and B only:

$$y_t = f(M, B) \qquad (3)$$

which, following a dimensional analysis leads to:

$$\frac{y_t}{d\mathsf{F}} = \text{Constant} \qquad (4)$$

Similar analyses lead to the following expressions for the other major jet geometric factors:

$$\frac{y_t}{d\mathsf{F}} = 2.2;$$
$$\frac{x_i}{d\mathsf{F}} = 2.4;$$
$$\frac{x_n}{d\mathsf{F}} = 9.0; \qquad (5)$$
$$\frac{y_L}{d\mathsf{F}} = 0.7$$

and for dilution:

$$\frac{S_i}{\mathsf{F}} = 1.6; \qquad (6)$$
$$\frac{S_n}{\mathsf{F}} = 2.6$$

where the values of the constants are taken from Roberts et al. (1997). The variables in Eqs. 5 and 6 are defined in Figure 1: y_t is the terminal rise height, xi the location of the jet impact point (and location of the minimum dilution on the lower boundary), x_n the length of the near field, y_L the thickness of the spreading layer, S_i the dilution at the impact point, and S_n the near field dilution (termed the ultimate dilution in Roberts et al., 1997). Eqs. 5 and 6 apply when the jets are fully turbulent, i.e. the jet Reynolds number, $\mathsf{Re} = ud/\nu$ where ν is the kinematic fluid viscosity is greater than about 2000, and the Froude number is greater than about 20, when the dynamical effect of the source volume flux becomes negligible.

2.1.2 Multiple Jets

Consider now the "conventional" multiport diffuser shown in Figure 2 (with discharge either from one or both sides). The port spacing is s. For this case, all of the constants on the right hand sides of Eqs. 5 and 6 become functions of $s/d\mathsf{F}$:

$$\frac{y_t}{d\mathsf{F}} = f\left(\frac{s}{d\mathsf{F}}\right);$$
$$\frac{x_i}{d\mathsf{F}} = f\left(\frac{s}{d\mathsf{F}}\right);$$
$$\frac{x_n}{d\mathsf{F}} = f\left(\frac{s}{d\mathsf{F}}\right); \qquad (7)$$
$$\frac{y_L}{d\mathsf{F}} = f\left(\frac{s}{d\mathsf{F}}\right);$$
$$\frac{S_i}{\mathsf{F}} = f\left(\frac{s}{d\mathsf{F}}\right);$$
$$\frac{S_n}{\mathsf{F}} = f\left(\frac{s}{d\mathsf{F}}\right)$$

The effect of the port spacing is therefore entirely encapsulated in the dimensionless parameter $s/d\mathsf{F}$.

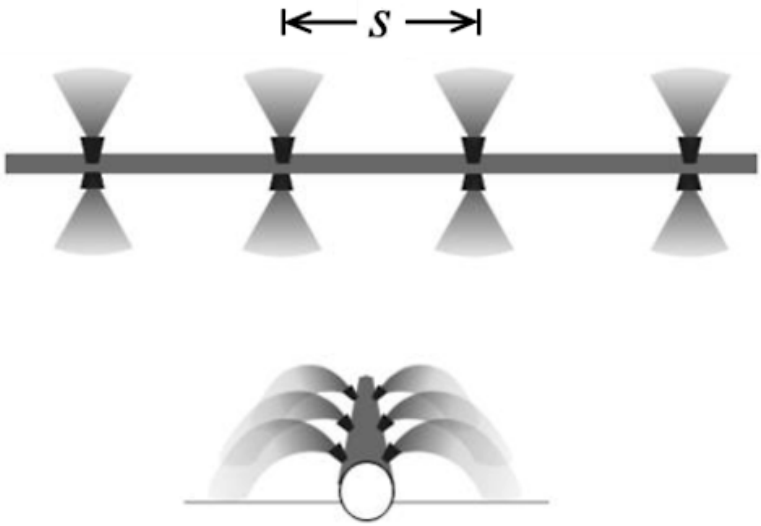

Figure 2. Multiport dense effluent diffuser.

Eq. 7 has two asymptotic solutions. For $s/d\mathsf{F}>>1$. the ports are widely spaced and the jets do not merge or interfere. In this case, the solutions should approach the single jet Eqs. 5 and 6. For $s/d\mathsf{F}<<1$, the jets are very close together and behave as if emitted from a line, or slot, source. In that case, the relevant discharge parameters are not the individual jet momentum and buoyancy fluxes, but the volume, momentum, and buoyancy fluxes per unit diffuser length, q, m, and b:

$$q = \frac{Q_T}{L}; \quad m = uq; \quad b = g_o' q \qquad (8)$$

where Q_T is the total discharge from the diffuser and L the diffuser length. The analysis analogous to Eq. 3 for a line source is then:

$$y_t = f\left(m, b\right) \qquad (9)$$

which, following a dimensional analysis becomes:

$$\frac{y_t b^{2/3}}{m} = \text{Constant} \qquad (10)$$

For a long diffuser $b = B/s$ and $m = M/s$ and it can be shown that Eq. 10 becomes, after some manipulation, and using the definition of Froude number, Eq. 2:

$$\frac{y_t}{d\mathsf{F}} = C_1 \left(\frac{s}{d\mathsf{F}}\right)^{-1/3} \qquad (11)$$

Similar arguments apply to the other geometrical parameters, so:

$$\begin{aligned}
\frac{y_t}{d\mathsf{F}} &= C_1 \left(\frac{s}{d\mathsf{F}}\right)^{-1/3}; \\
\frac{y_L}{d\mathsf{F}} &= C_2 \left(\frac{s}{d\mathsf{F}}\right)^{-1/3}; \\
\frac{x_i}{d\mathsf{F}} &= C_3 \left(\frac{s}{d\mathsf{F}}\right)^{-1/3}; \\
\frac{x_n}{d\mathsf{F}} &= C_4 \left(\frac{s}{d\mathsf{F}}\right)^{-1/3}
\end{aligned} \qquad (12)$$

and for dilution:

$$\frac{S_i}{\mathsf{F}} = C_5\left(\frac{s}{d\mathsf{F}}\right)^{1/3};$$
$$\frac{S_n}{\mathsf{F}} = C_6\left(\frac{s}{d\mathsf{F}}\right)^{1/3} \qquad (13)$$

where C1 through C6 are experimental constants. These equations should apply to diffusers with discharges from one or both sides, although the values of the constants may be different. As the jets are moved closer together, Eq. 12 implies that the rise height and other geometrical parameters increase, and Eq. 13 implies that the dilution decreases.

We would expect a transition between the single jet solutions ($s/d\mathsf{F} << 1$) and line jet solutions ($s/d\mathsf{F} >> 1$) to occur at $s/d\mathsf{F} \sim O(1)$. Systematic experiments were performed to investigate the nature of these relationships.

2.2 Flowing Currents

Flows with currents are considerably more complex. Fundamental studies on vertical jets are presented in Gungor and Roberts (2009). The effect of the current is determined by the dimensionless parameter $u_r\mathsf{F}$ where $u_r = u_a/u$ is the ratio of the ambient current speed to the jet exit velocity. If $u_r\mathsf{F} >> 1$, then the jet is strongly bent over by the current; if $u_r\mathsf{F} << 1$, then the current has little effect on the jet.

With a cross flow, Eq. 7 becomes, for example:

$$\frac{S_i}{\mathsf{F}} = f\left(\frac{s}{d\mathsf{F}}, u_r\mathsf{F}\right);$$
$$\frac{y_t}{d\mathsf{F}} = f\left(\frac{s}{d\mathsf{F}}, u_r\mathsf{F}\right); \qquad (14)$$
$$\frac{x_n}{d\mathsf{F}} = f\left(\frac{s}{d\mathsf{F}}, u_r\mathsf{F}\right)$$

Generally dilution increases and rise height decreases with increasing current speed.

3. EXPERIMENTAL PROCEDURE

3.1 Introduction

The experiments were conducted as shown schematically in Figure 3.

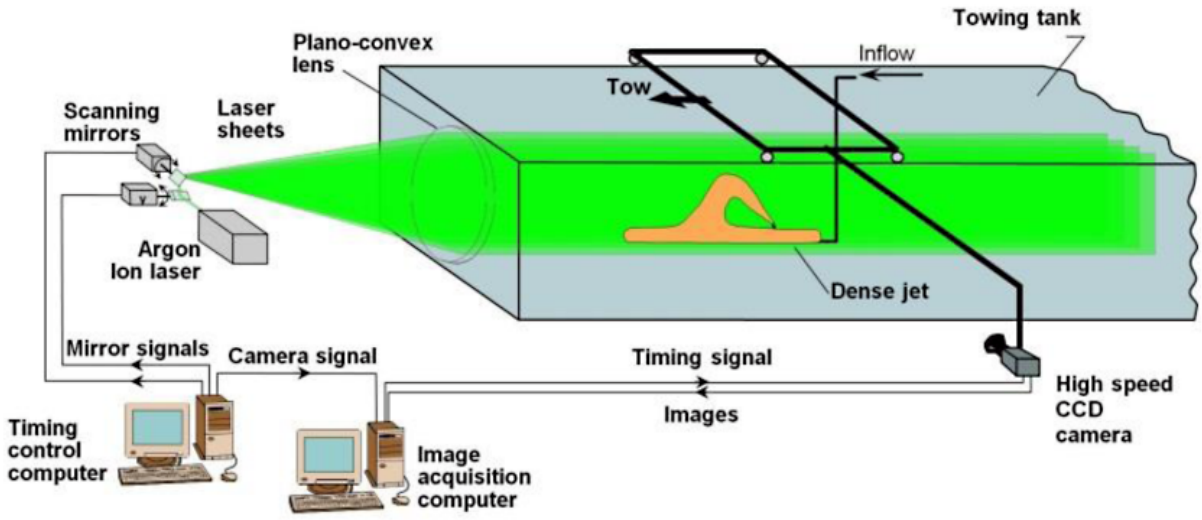

Figure 3. Schematic depiction of experimental procedure.

A three-dimensional Laser-Induced Fluorescence system (3DLIF) was used to measure the spatial evolution of the mixing processes and dilution. The experiments were performed in the Environmental Fluid Mechanics Laboratory at the Georgia Institute of Technology in a tank with glass walls 6.10 meters (m) long by 0.91 m wide by 0.61m deep.

The 3DLIF system has been described in several publications, for example Gungor and Roberts (2009), and the experimental configuration is the same as shown in figure 3 of that paper except that the diffuser models are multiport diffusers. The only change from the previous 3DLIF system is that the camera is an upgraded digital charge-coupled device (CCD) camera, Imperx Bobcat with 640 by 480 pixels. In the present experiments, the width of the frame (the field of view) was about 750 millimeters (mm), therefore the pixel resolution is 750/640=1.2 mm. The camera was operated in 8-bit (256 gray levels) mode for which the maximum imaging rate is 260 frames/sec. The images were streamed to an IO Industries DVR Express Core storage device and then to a PC hard drive for further analyses.

The system consists of two fast scanning mirrors that drive the beam from an Argon-Ion laser through the flow in a programmed pattern. The mirrors create vertical light sheets about one mm wide that are swept horizontally through the flow at high speed. The system is controlled by two computers, one for overall timing control, and one for image capture. A small amount of a fluorescent dye (Rhodamine 6G) is added to the inflow; the laser causes the dye to fluoresce, and the emitted light is captured by the CCD camera. The first mirror sweeps the beam down and back while the camera is exposing (i.e., the shutter is “open”). The second mirror then moves the beam a small distance horizontally, the previous frame is downloaded, the camera buffer cleared, and the next exposure begins. This is repeated so that multiple vertical “slices” through the flow are obtained. After a predetermined number of slices, the beam returns to the starting

point and the cycle starts again. The experimental parameters were varied to optimize them for each experiment, but a typical imaging rate was 100 frames per second, with 40 vertical slices spaced about 7 mm apart.

The images were corrected pixel-by-pixel for sensor response, lens luminance variation (vignetting), and laser attenuation through the clear water, dye, and salt. The accuracy of the dilution measurements thus obtained is about ±10% (Tian 2002). Finally, the multiple slices through the flow field are regenerated, using image processing techniques, into three-dimensional images of the flow field.

3.2 Procedure

The general experimental procedures are similar to those in Gungor and Roberts (2009) and the method of extracting tracer concentrations from the images are discussed in detail in Tian and Roberts (2003). The receiving water was uniform density freshwater that was dechlorinated and filtered to improve clarity. The effluent consisted of dechlorinated water with the addition of salt (NaCl) for density control and Rhodamine 6G fluorescent dye as a tracer. Typical dye concentrations in the diluted jet ranged from about one to 100 μg/l. Before each experiment and after the tow tank had been filled, two rectangular cylinders containing known dye concentrations were placed at the left and right extents of the field of view and images obtained. This was repeated for several known dye concentrations. The relationship between dye concentration and pixel response (a digital number that ranges from 0 to 255) is linear and the slope was obtained by a linear regression fit to the data. The attenuation coefficient for the clear water was obtained from the decrease in fluorescence intensity measured by the two cells placed a known distance apart. The spatial scale (magnification factor) was obtained by imaging a ruler placed on the central laser sheet plane, and the scale for off-center images was obtained by simple geometric relationships, Tian (2002). The flow was begun, and after waiting for a few minutes scanning begun. Data were typically obtained for about 60 to 90 seconds.

The parameters were chosen to cover a wide range typical of those expected for oceanic brine diffusers. All experiments were conducted with nozzles oriented upwards at 60° to the horizontal. Various diffusers were tested with either 1, 4, 7, or 22 nozzles discharging to one or both sides of the diffuser. For the experiments with one nozzle, the port diameter was 3.25 mm, for four and seven ports it was 1.93 mm, and for 22 ports it was 2.79 mm.

Each experimental data set consists of millions of sample points, each one sampled at about 0.4 hertz (Hz). This leads to data files of several gigabytes for each experiment, and considerable processing and computer graphics are needed to analyze and visualize the results.

3.3 Parameters Tested

A summary of the experimental parameter range completed is given in Table 1. It can be seen that a very wide range of parameters, covering most cases of practical outfalls have been investigated.

Table 1. Summary of Ranges of Experimental Parameters Tested

Description	Densimetric Froude number, F	Port spacing parameter, $s/(dF)$	Current speed parameter, $u_r F$
Multiport diffuser in stagnant current	8.5 - 110	11.7 - 0.45	0
Multiport diffuser with discharge from one side in co-flowing current	12.3 - 113	7.71 - 0.26	0.67 – 7.95
Multiport diffuser with discharge from one side in counter-flowing current	20.4 - 113	7.71 - 0.26	7.95 - 0.67
Multiport diffuser with discharge from both sides in flowing current (blocked and unblocked)	8.79 - 46.2	0.93 - 4.14	0.9 - 4.68
Rosette diffuser in stagnant current (1 and 3 rosettes)	20.8 – 66.7	0.36 – 2.22	0
Rosette diffuser in flowing current (1 and 3 rosettes)	29.1 – 83.3	0.51 – 14.5	1.02 - 3.88

4. EXPERIMENTAL RESULTS

4.1 Multiport Diffuser in Stationary Currents

4.1.1 Experiments

The experimental conditions and results are summarized in dimensionless form in the Appendix, Table A1.

4.1.2 Results

A typical time-averaged image of jets from a diffuser with discharge from both sides is shown in Figure 4. It shows the outer surface of the jets as a semi-transparent iso-surface. A vertical plane though one of the jets shows the tracer concentration levels (corresponding to salinity in the prototype diffuser) as false colors. The levels are high near the jet but reduce due to turbulent entrainment and mixing before the jet impacts the sea bed.

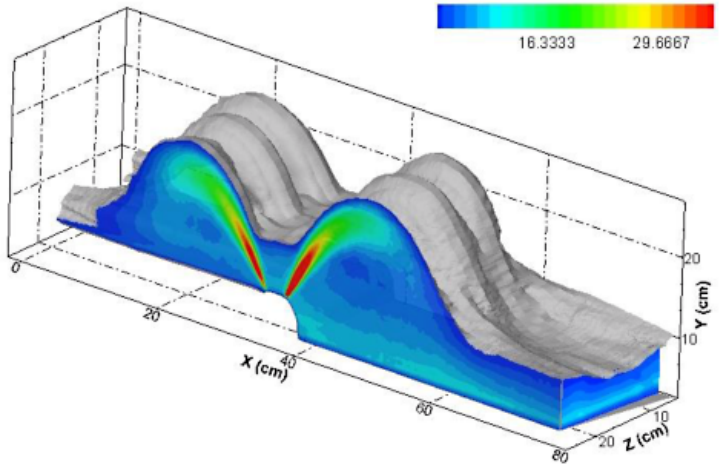

Figure 4. Three-dimensional time-average image of flow from a multiport diffuser. F = 46, *s/d*F = 0.6.

For each experiment, the time-average concentration field was computed using the methods discussed above and in previous papers. The main geometrical parameters shown in Figure 1 were then computed: the terminal rise height y_t, the location of impact dilution x_i, the location of the end of the near field x_n, and the impact dilution S_i and near-field dilution Sn. Results for near field dilution are shown in Figure 5 and for rise height in Figure 6. Also plotted on these graphs are the expected asymptotic solutions for point sources (s/dF >> 1, Eqs. 5 and 6) and line sources (s/dF << 1, Eqs. 12 and 13). Results for diffusers with discharge from one side are shown with solid symbols, and for discharge from both sides with open symbols.

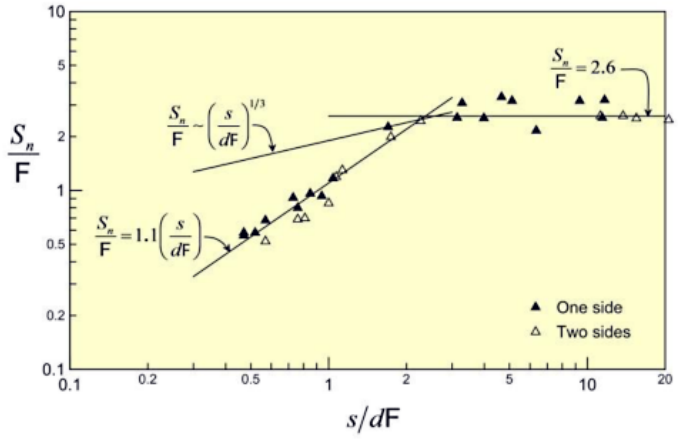

Figure 5. Effect of port spacing on near field dilution.

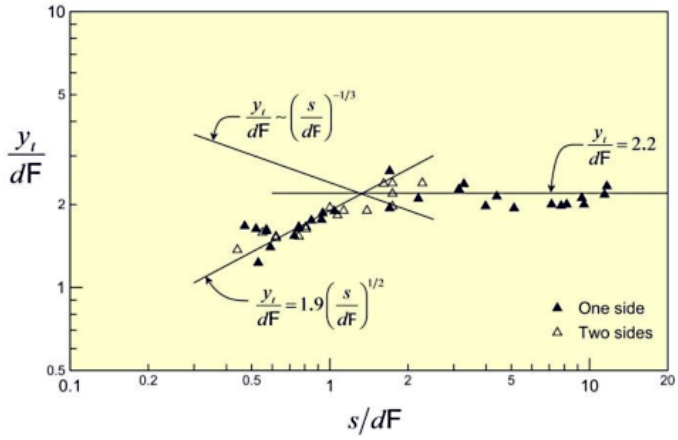

Figure 6. Effect of port spacing on rise height.

Generally, the data follow the expected point source asymptotic solutions for $s/dF > \sim 2$. For smaller spacings they do not follow the expected line source solutions, however.

All of the geometrical parameters, y_t, x_i, and x_n, actually decrease as the spacing decreases rather than increasing as predicted by Eq. 12. The dilutions S_i and S_n, do decrease with spacing as expected, but they decrease at a much faster rate than predicted by Eq. 13. Even allowing for experimental scatter, dilutions for diffusers with ports on both sides seem to be systematically slightly lower than for diffusers discharging on one side (for otherwise similar values of F and s/dF).

Empirical equations were fitted to the results for $s/dF < \sim 2$:

The increase in dilution from the impact point to the end of the near field is about 60% for non-merged jets and 40% for merged jets. These are similar to the observations for single jets in Roberts et al. (1997). No previous results have been reported for near field dilutions of merged dense jets, but the increase in dilution from the impact point to the near field for positively buoyant fully merged (line plume) discharges was reported by Tian and Roberts (2004) to be about 20%.

The reasons that the results do not follow those predicted for slot jets were evident from unsteady animations of the results that began from initiation of discharge. It was observed that the closely-spaced jets initially rose much higher, and the rise height then decreased with time to approach those shown in Figure 6. This was caused by the falling jets being re-entrained by the rising jets. It can be seen in the comparisons of two experiments that have similar jet parameters (same F) but different port spacing. The jets merge and the cavity between the rising and falling jets became filled as can be seen in Figure 4. The entraining flow cannot penetrate through the jets to the interior, starving them and reducing dilution. This

"sucking in" of the jets also resulted in reduction of the jet impact point distance x_i and the length of the near field x_n compared to similar single jets. This effect is also known as the Coanda effect.

Clearly, the spacing must be sufficient that entraining flow is available for the jets. This apparently occurs when $s/d\mathsf{F} > 2$.

4.1.3 Discussion

The Coanda effect on buoyant jets from diffusers has been observed and noted in several contexts. It arises from the "Bernoulli" effect whereby the presence of a nearby boundary or adjacent jet causes a change in the entrained flow pattern that results in a pressure force that moves the jet towards the boundary or to the other jet. If there is a boundary, such as the bed or water surface, the jet can deflect towards it and cling to it. If there are adjacent jets, they can be thought of as trying to mutually entrain each other.

Coanda effects in the present case of multiple merging dense jets interact to cause the reduction in rise height and more rapid reduction in dilution that was observed. The major one is a "self-Coanda" effect between the rising part of the jet and the descending part whereby the rising jet attempts to re-entrain itself. This effect is exacerbated by the merging of the jets to a virtually impenetrable wall (see Figure 4) that prevents the flow of entraining water to the central core—"starving" them and forming an almost closed recirculation zone therein that does not occur with a single jet. This exacerbates the curvature as the inward faces attempt to entrain clear water. In addition, there is a Coanda attraction to the lower boundary, although this is probably less of a factor than the self-Coanda effect. All of these factors reduce the rise height and cause the jet trajectory to be more sharply curved and shorter, and also causes the impaction point to contract inwards. The shorter trajectory further reduces dilution by reducing the area of the outer surface available for entrainment. The Coanda effect between adjacent jets (dynamic interaction) is less important because it cancels out, except for the end jets.

It would be expected that the dimensional arguments presented for slot jets (Eqs. 12 and 13) would apply to the early stages of the jet flow when the flow reaches its maximum rise height, although this hypothesis was not tested.

Further results for this case are presented in the paper to be published in the Journal of Hydraulic Engineering.

4.2 Multiport Diffuser in Co-Flowing Currents

4.2.1 Experiments

These experiments were conducted with diffusers discharging to one side with a co-flowing current (in the same direction as the jets). 74 experiments with Froude numbers ranging from 12.3 to 113, four port spacings (s = 5.72, 9.8, 19.6, 91 cm), various current speeds (u_a = 1.8 to 10.4 cm/s), $s/d\mathsf{F}$ from 0.26 to 7.71 and $u_r\mathsf{F}$ from 0.67 to 7.95 were conducted. 32 experiments were conducted with 7 port diffusers, 19 with 4 port diffusers, 12 with 2 port diffusers, and 11 with single ports. As shown in Figure 7, four parameters: the maximum rise height, dilution at maximum rise height, impact point location, and impact point dilution were computed.

As discussed in Sections 2.1 and 2.2, the effect of port spacing and current speed are expressed by the dimensionless parameters $s/d\mathsf{F}$ and $u_r\mathsf{F}$ respectively (see Eq. 14). The results below are therefore plotted against these parameters.

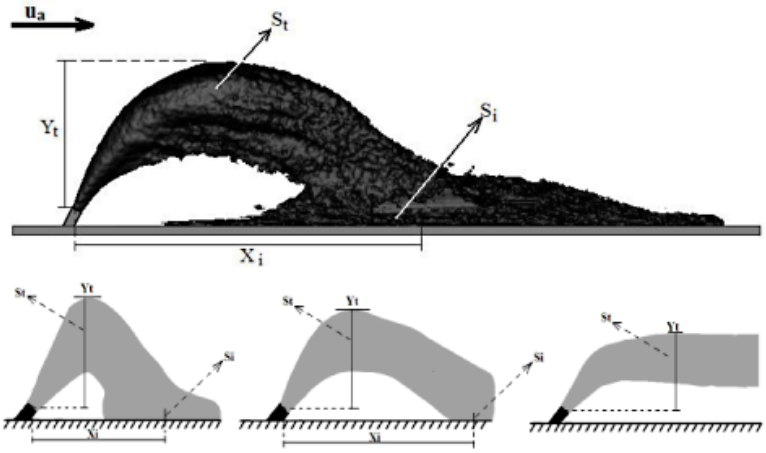

Figure 7. Flow characteristics of multiport discharge in co-flowing current.

4.2.2 Results

Flow images for single ports are shown in Figure 8. Comparisons between the flows for single and closely merged jets approximating line sources are shown in Figure 9.

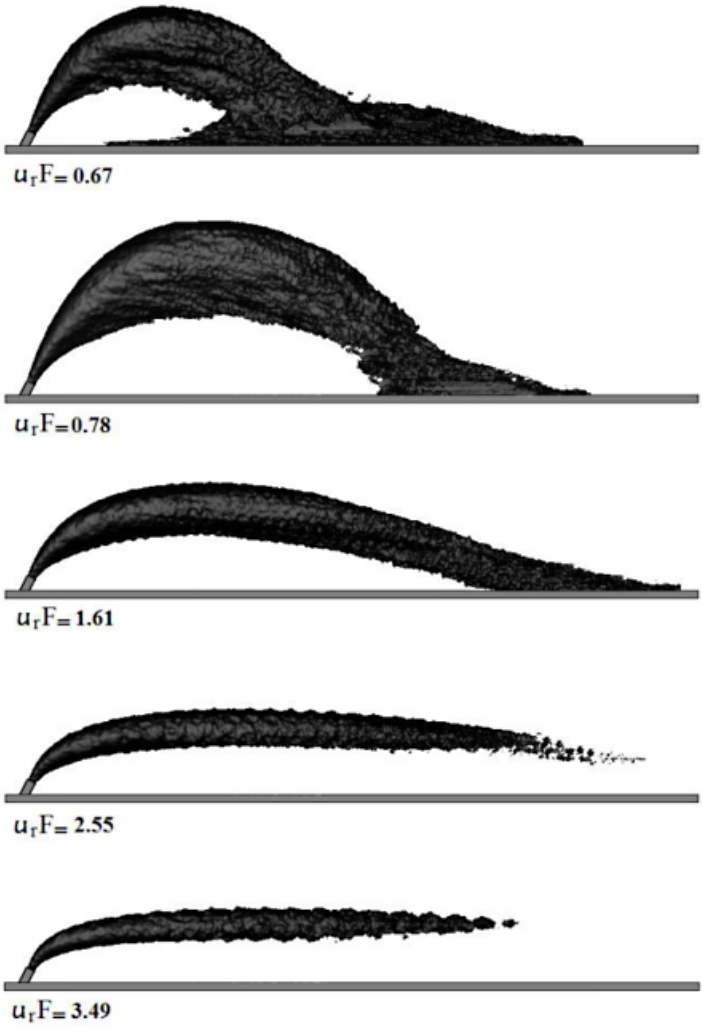

Figure 8. Discharges in co-flowing currents for single port discharges (*s*/*d*F > 1.91).

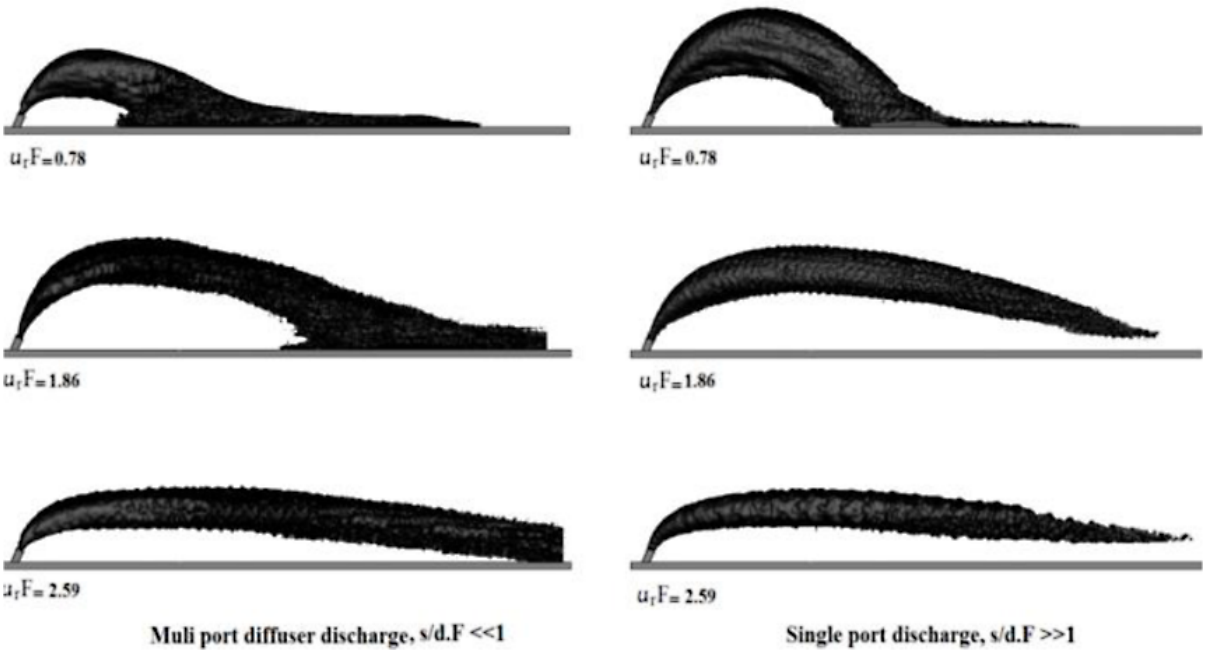

Figure 9. Discharges in co-flowing currents for line sources (*s/d*F < 0.62) and point sources (*s/d*F > 1.91).

The methodology for determining the maximum rise height is shown in Figure 10. It was defined as the location where the local concentration is 10% of the jet centerline value in the vertical plane through the maximum rise height. The geometrical parameters, maximum rise height y_t and location of impact point x_i are shown in Figures 11 and 12. The dilutions at the terminal rise height S_t and at the impact point S_i are shown in Figures 13 and 14. In these graphs the results are plotted versus s/dF for approximately constant values of u_rF.

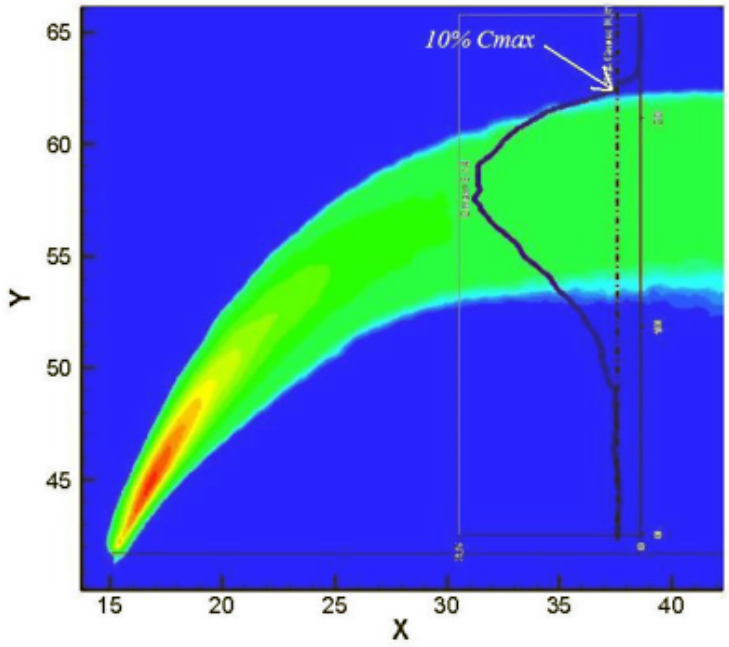

Figure 10. Methodology for finding maximum rise height, y_t.

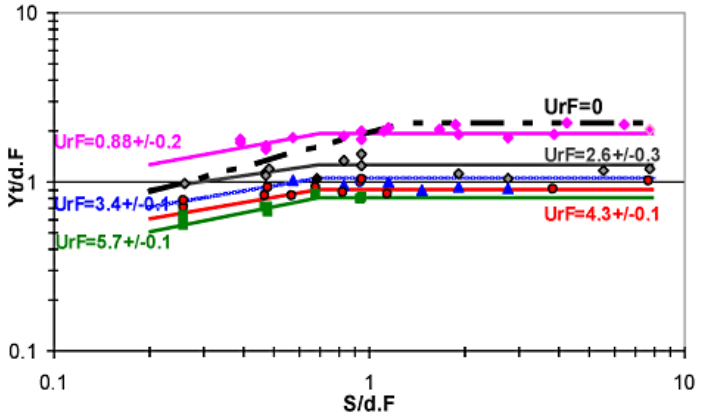

Figure 11. Maximum rise height for multiport diffuser in co-flowing currents.

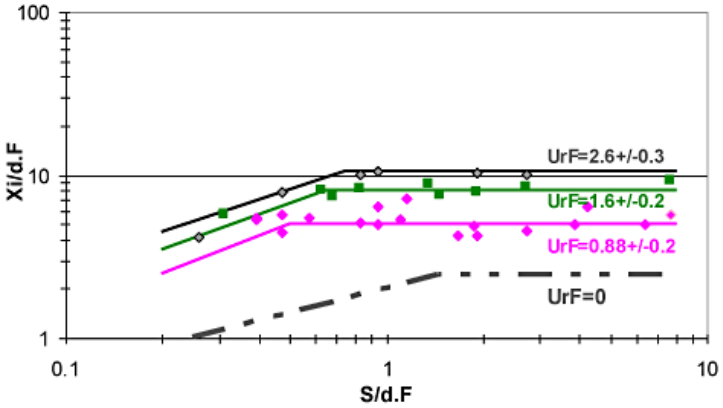

Figure 12. Location of impact point for multiport diffuser in co-flowing current.

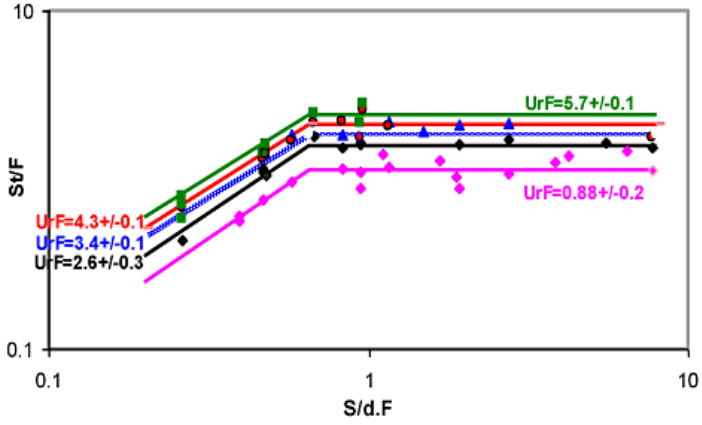

Figure 13. Dilution at maximum rise height for multiport diffuser in co-flowing current.

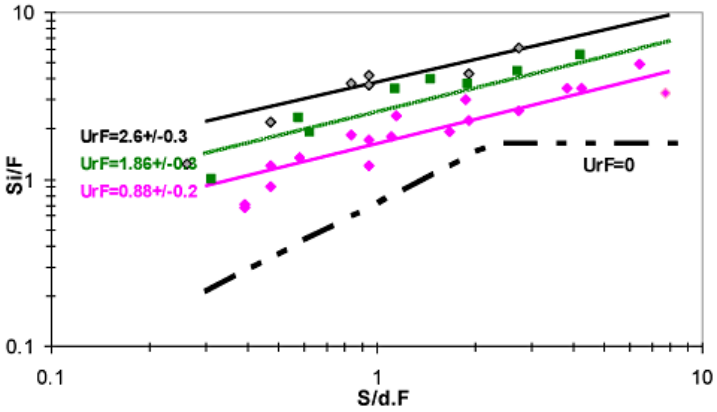

Figure 14. Dilution at impact point for multiport diffuser in co-flowing current.

In addition, downstream variations of jet centerline trajectory, jet width, and dilution were investigated. To accomplish this, concentration profiles perpendicular to the jet centerline at various downstream distances were extracted from the flow images. The x and y coordinates of the locations of maximum concentration (the centerline trajectory) in each profile were then found. Profile maximum concentration and the jet widths (defined as where the concentration is 10% of the maximum) were also identified in these profiles. The centerline trajectories for various current speeds (different u_rF) for closely-spaced jets (s/dF << 1) are shown in Figure 15 and for single jets (s/dF >> 1) in Figure 16.

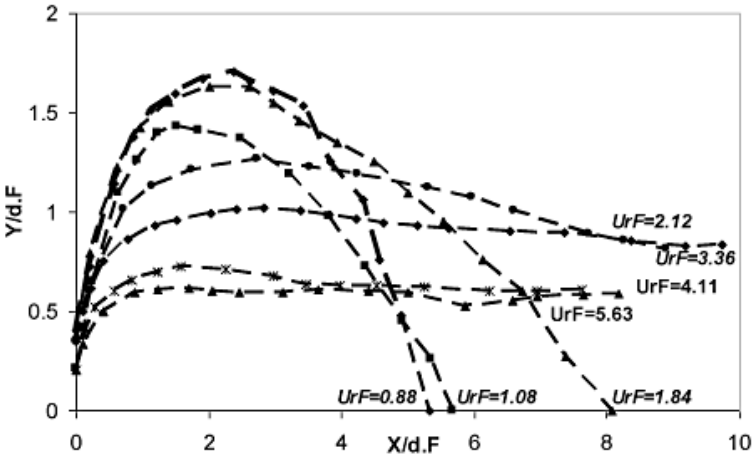

Figure 15. Centerline trajectory for line source (*s/d*F < 0.62) in co-flowing current.

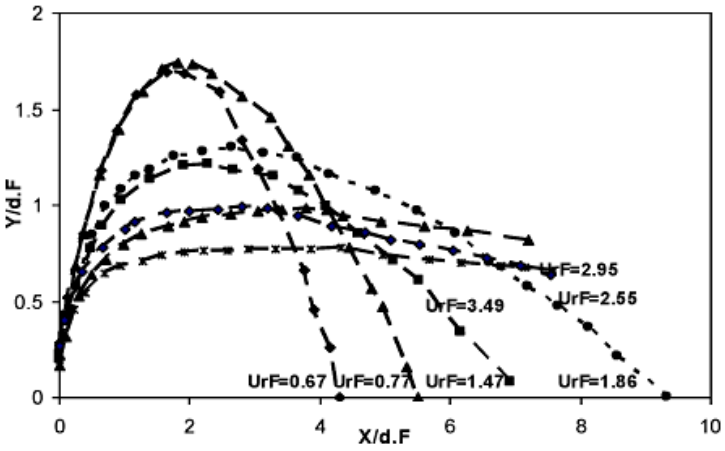

Figure 16. Centerline trajectory for point source (*s/d*F > 1.91) in co-flowing current.

The trajectories for line (colored) and point sources (black) are compared in Figure 17. The jets from the line sources impact the bottom closer to the diffuser than those from the point sources. Merging changes the flow trajectory for otherwise similar jets for low current speeds, but similar strong influences of merging on centerline trajectories were not observed for faster currents.

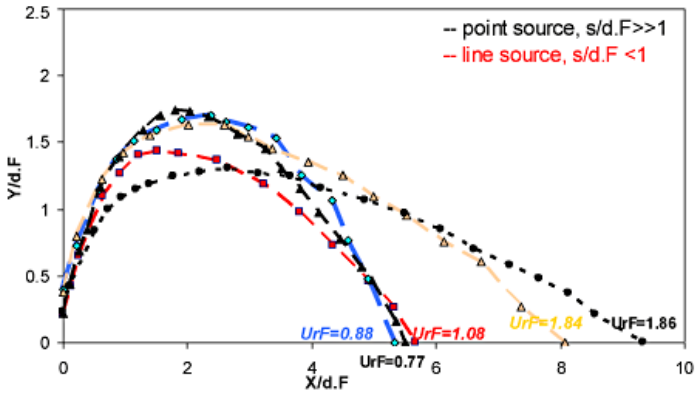

Figure 17. Centerline trajectories of line source (colored line) and point source (black line).

An example of the downstream variation of a centerline trajectory and upper and lower jet widths is shown in Figure 18.

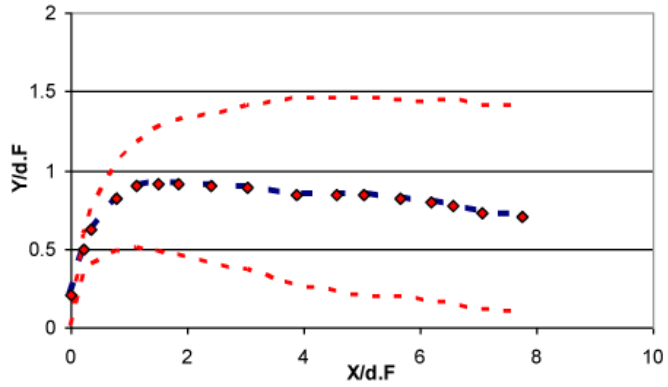

Figure 18. Centerline trajectory and its upper and lower extents for the Exp3-14 March, u_rF = 2.59, s/dF = 0.46.

The variations of jet width for various ambient currents are shown in Figure 19. As can be seen, when the current speed increases, the width decreases.

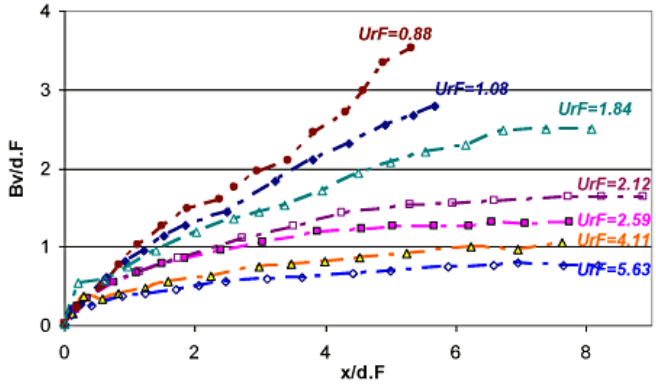

Figure 19. Variation of downstream jet width for various current speeds.

Centerline dilution is also plotted for experiments with the same Froude number and various current speeds in Figure 20. The dilutions are not strongly affected by the current when close to the source, but dilution increases farther away from the source as the current speed increases.

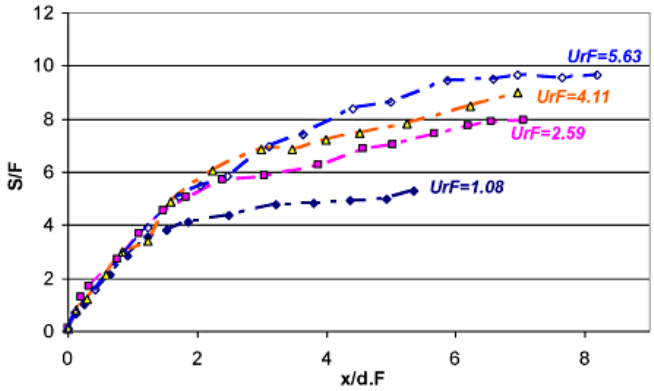

Figure 20. Variation of downstream dilution for same Froude number at various current speeds.

4.2.3 Discussion

The maximum rise height decreases as u_rF increases (Figure 11). A break point occurs near s/dF ≈ 0.7 for most u_rF. Beyond this point, the maximum rise height does not change with s/dF, and the flow behaves like a point source.

As shown in Figure 12, the dilution at the maximum rise height increases when u_rF increases. Break points were again observed for s/dF ≈ 0.7; beyond this point, dilution does not change with s/dF, and the flow approximates a point source. The impact point location (Figure 13) generally moves farther downstream as u_rF increases. Again, the break point occurs at s/dF ≈ 0.7. The impact point dilution (Figure 14) increases with u_rF. It also increases with s/dF, which indicates that some merging occurs at some point downstream for smaller s/dF. The trajectories (Figures 15 and 16) of a line source (s/dF << 1) is different from a point source (s/dF >> 1). Generally, the trajectory is longer for point sources (Figure 17). As shown in Figure 18 and 19, the flow width increases downstream when the Froude number (u_rF) decreases. Finally, Figure 20 shows that downstream dilution increases as u_rF increases.

4.3 Multiport Diffuser in Counter-Flowing Currents

4.3.1 Experiments

These experiments were conducted with diffusers discharging to one side with a counter-flowing current (opposing the jets). The Froude number, F, ranged from 12.2 to 113, port spacings s were 5.72, 9.80, 19.6, 91.0 centimeters (cm), and ambient current speeds, u_a from 1.76 to 10.41 centimeters per second (cm/s). 63 experiments were conducted, 26 with a 7 port diffuser, 14 with a 4-port diffuser, 11 with a 2-port diffuser, and 12 with single ports, s/dF ranged from 0.26 to 7.74 and u_rF from 0.67 to 7.95.

Images of flows for a single jet discharge for different u_rF are shown in Figure 21 and some comparisons between multiport and single jet discharges in Figure 22.

4.3.2 Results

Four main parameters were measured as shown in Figure 23: the maximum height rise, y_t, dilution at the maximum height rise, S_t, impact point location, x_i, and dilution at the impact point, S_i. These parameters were obtained using the same methods as for the co-flow experiments.

The results are plotted in dimensionless form according to Eq. 14 in Figures 24 to 27. In these figures, changes in flow properties with nozzle spacing are observed. Straight lines are fitted to the results that indicate a break point where port spacing no longer influences these flow properties.

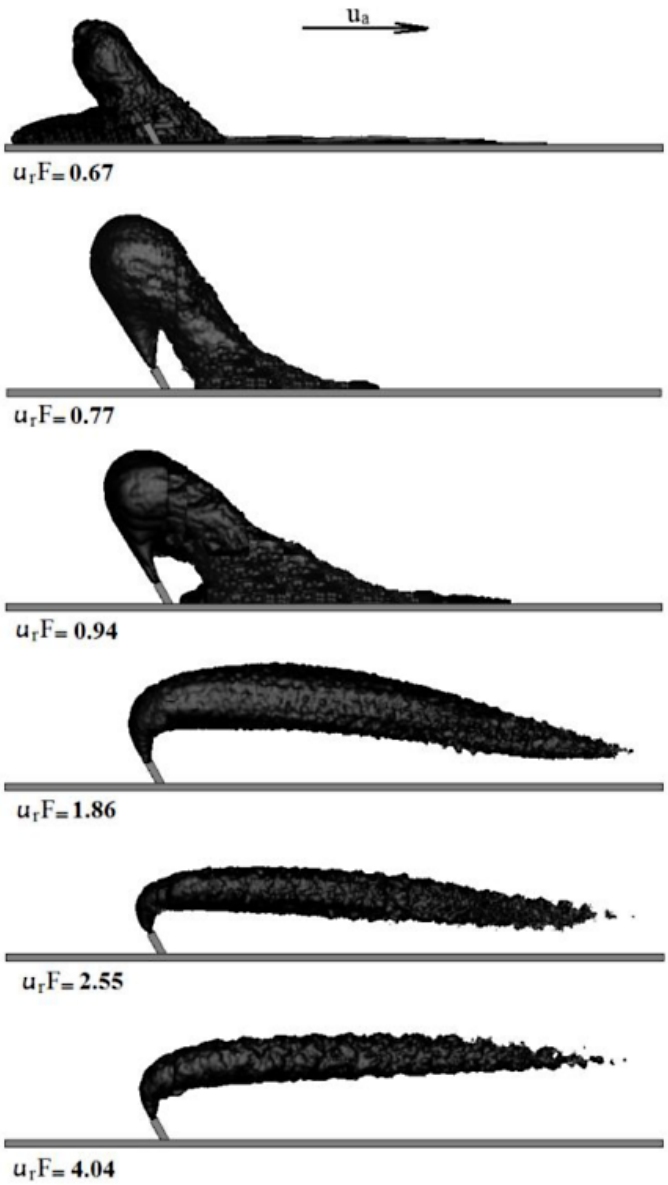

Figure 21. Typical images of multiport counter-current discharges.

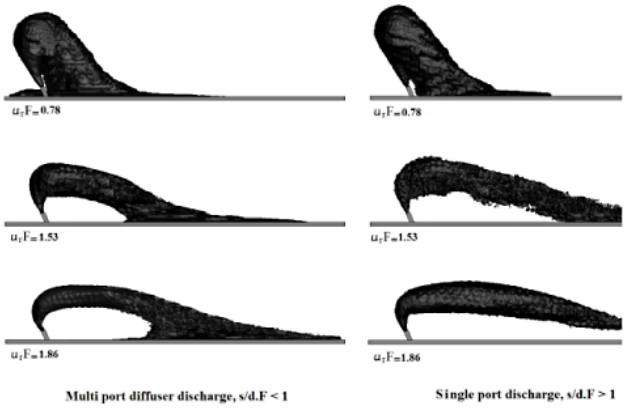

Figure 22. Comparisons of multiport and single port discharges in counter-flowing current.

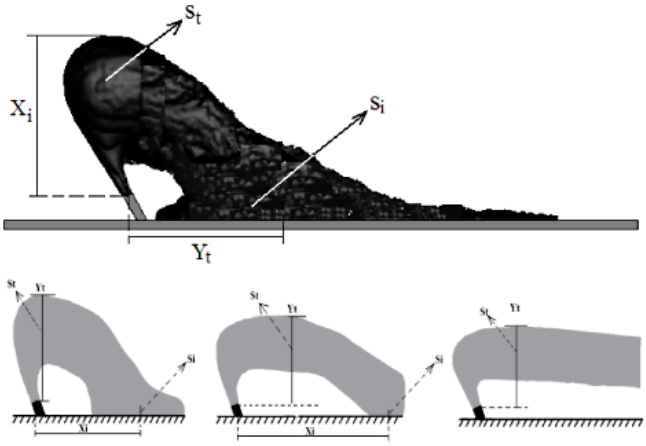

Figure 23. Main measured properties for discharges into counter-flow current.

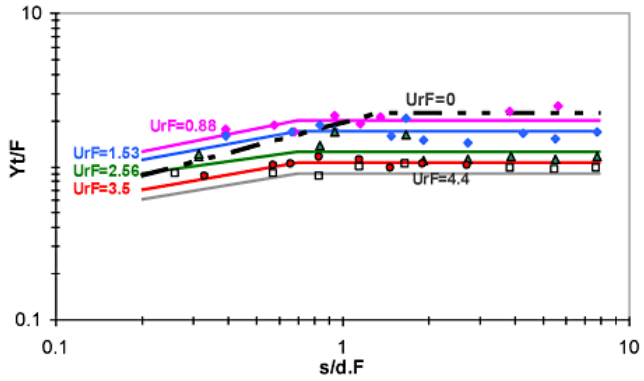

Figure 24. Maximum rise height in counter-flow.

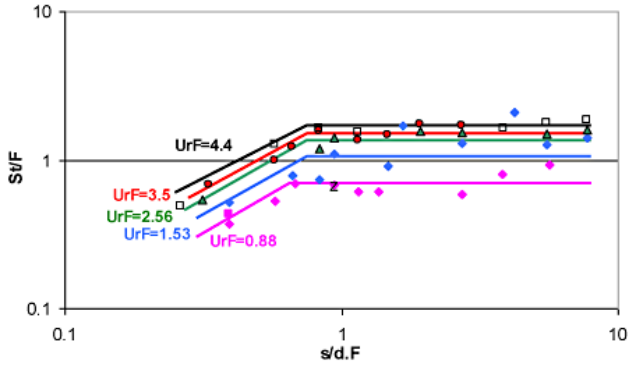

Figure 25. Dilution at maximum rise height in counter-flow.

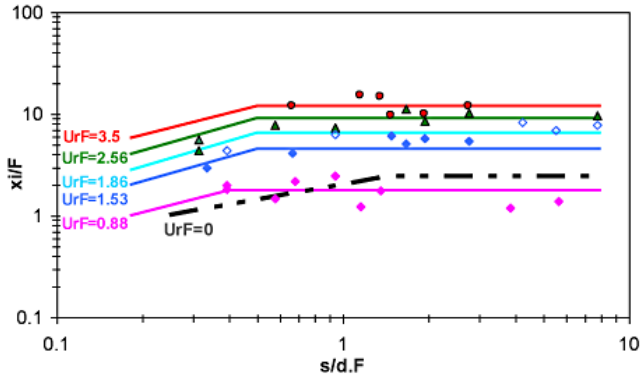

Figure 26. Location of impact point in counter-flow.

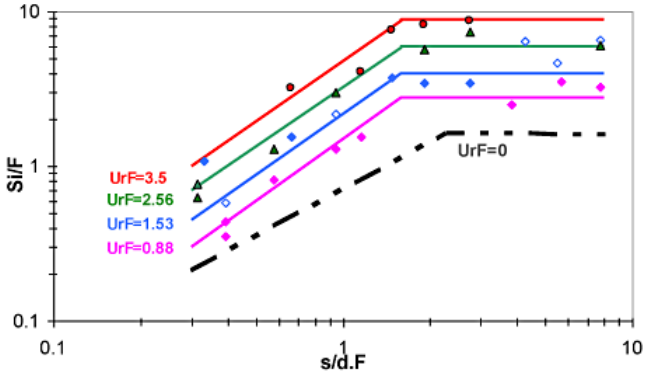

Figure 27. Dilution at impact point in counter-flow.

To better see the influence of port spacing on flow behavior, jet trajectories for the two limiting cases of port spacing were measured. The trajectory for a line source, $s/d_F >> 1$ (7 port diffuser) are plotted in Figure 28, and for a point source, $s/d_F << 1$, (single port discharge) in Figure 29.

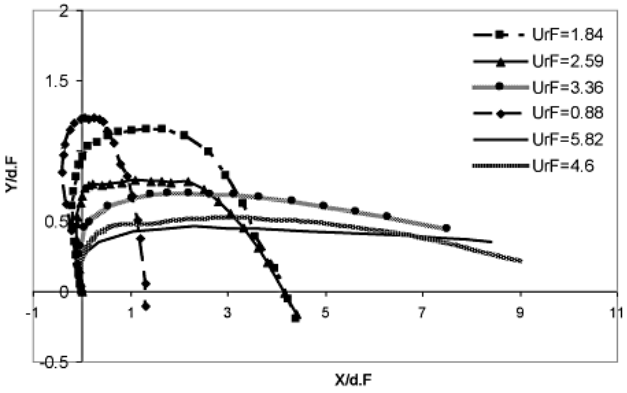

Figure 28. Centerline trajectory in counter flow for line sources ($s/d_F < 0.7$).

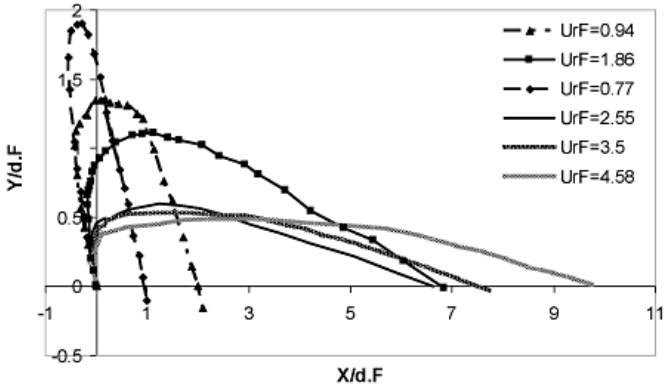

Figure 29. Centerline trajectory in counter flow for point sources ($s/d_F > 3.8$).

The trajectories are different. To compare them directly, trajectories with the same value of u_rF for point and line sources conditions are plotted together in Figures 30, 31, and 32. It can be seen that, for smaller u_rF, due to merging for a line source, the flow impacts the bed closer to the source than for a point source (Figures 30 and 31). The effect is less pronounced at higher current speeds, however, (Figure 32).

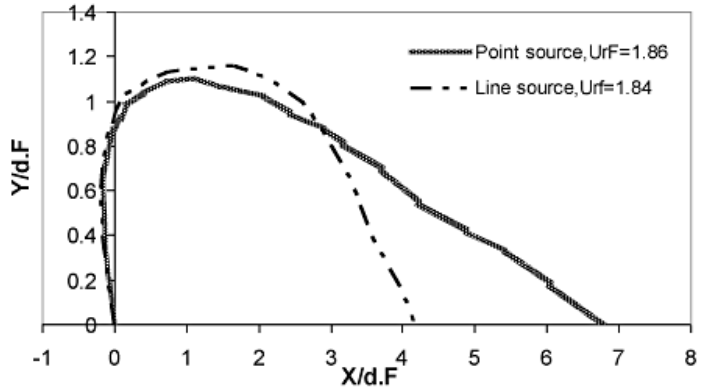

Figure 30. Flow trajectories for line and point sources in counter-flow, $u_rF \approx 1.8$.

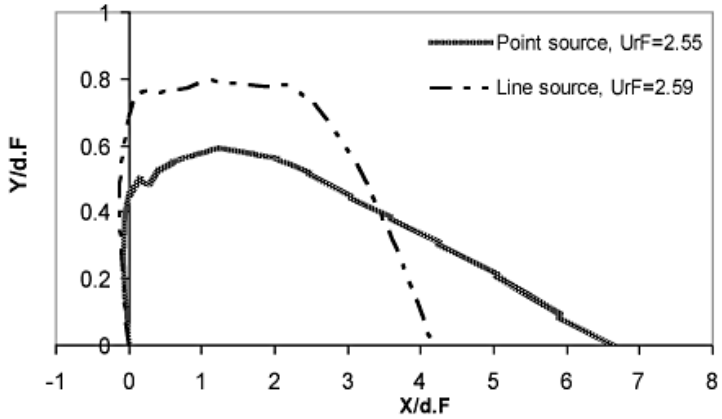

Figure 31. Flow trajectories for line and point sources in counter-flow, $u_rF = 2.6$.

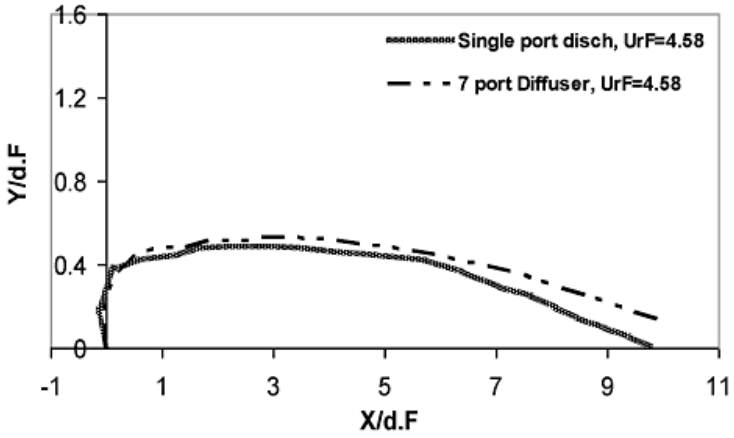

Figure 32. Trajectories for line and point sources in counter flow, u_rF ≈ 4.6.

4.3.3 Discussion

From these experiments on discharges into a counter flow, it can be concluded that:

The jet falls back directly onto itself for u_rF ≈ 0.67 (and probably less). For higher current speeds, the maximum rise height decreases when u_rF increases.

The maximum rise height and dilution depend on port spacing (s/dF). As observed in Figures 24 and 25, they increase with s/dF up to a break point around s/dF ≈ 0.7. Beyond this point, the flow properties no longer depend on s/dF, and the flows behave as a point source.

A break point was also observed in Figures 26 (s/dF ≈ 0.5) and 27 (s/dF ≈ 1.4) for the location of the impact point and the dilution there. They also show the influences of port spacing on flow properties at the impact point. Compared to co-flowing currents, the location and dilution of impact point in counter-flow has break points in the lower value of s/dF (s/dF ≈ 0.7 for impact point in co-flow).

Moreover, the difference in location of break point in figures developed for maximum rise height and impact point, the slope of line in the zone of line source are different for flow geometrical properties and dilution.

Comparisons of the flow trajectories for line and point sources show the influence of merging on flow trajectory. Point source flows impinge the bed farther downstream than do line sources.

4.4 Multiport Diffuser with Discharge from Both Sides into a Flowing Current

4.4.1 Experiments

The configuration for this case is shown in Figure 33.

A total of 62 experiments were conducted. Of these, 32 were conducted with a 1.3 cm gap between the diffuser bottom and the channel bed to allow flow underneath the diffuser, and 30 with no gap. These two conditions are referred to henceforth as "blocked" and "unblocked."

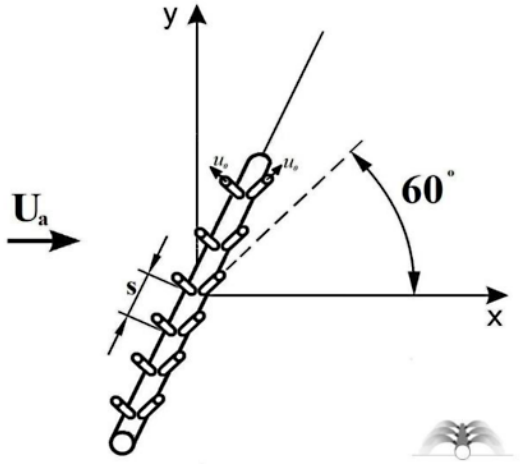

Figure 33. Schematic of two-sided diffusers with 60° nozzles.

The parameters ranges for these experiments are:

Blocked (30 experiments)
F: 8.79 to 46.2
*s/d*F: 0.93 to 4.14
u_rF: 0.9 to 3.42

Unblocked (32 experiments)
F: 8.79 to 46.2
*s/d*F: 0.93 to 4.14
u_rF: 0.9 to 4.68

The model diffuser was 86 cm long with 18 nozzles contained in 9 risers each with two ports. The ports were horizontally opposed, so one side of the diffuser discharges counter- flow and one co-flow to the current (see Figure 33).

4.4.2 Results

Some typical flow images are shown in Figure 34. First of all, a merging observed between co- and counter-flow in one riser and then, depending *s/d*F, merging on the sides. The flow behavior changes with current speed (u_rF). In this condition, we have both co- and counter flow that merge together downstream.

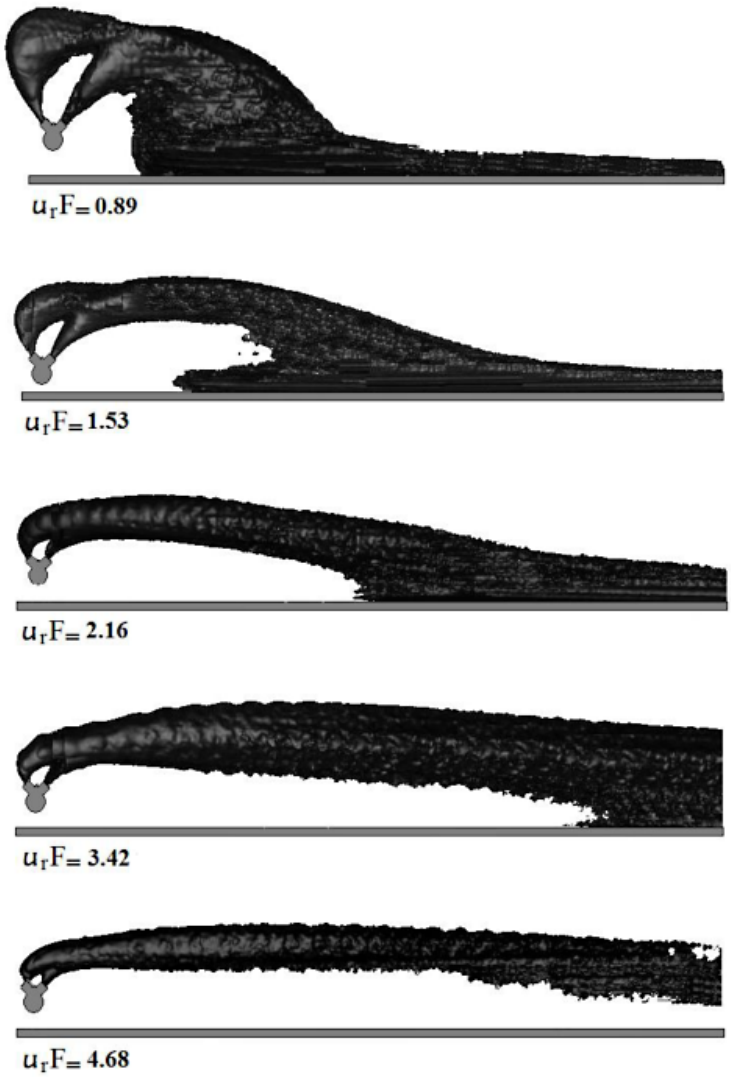

Figure 34. Typical flow images at various u_rF.

The flow is significantly impacted by the presence or absence of the gap, allowing flow under the diffuser.

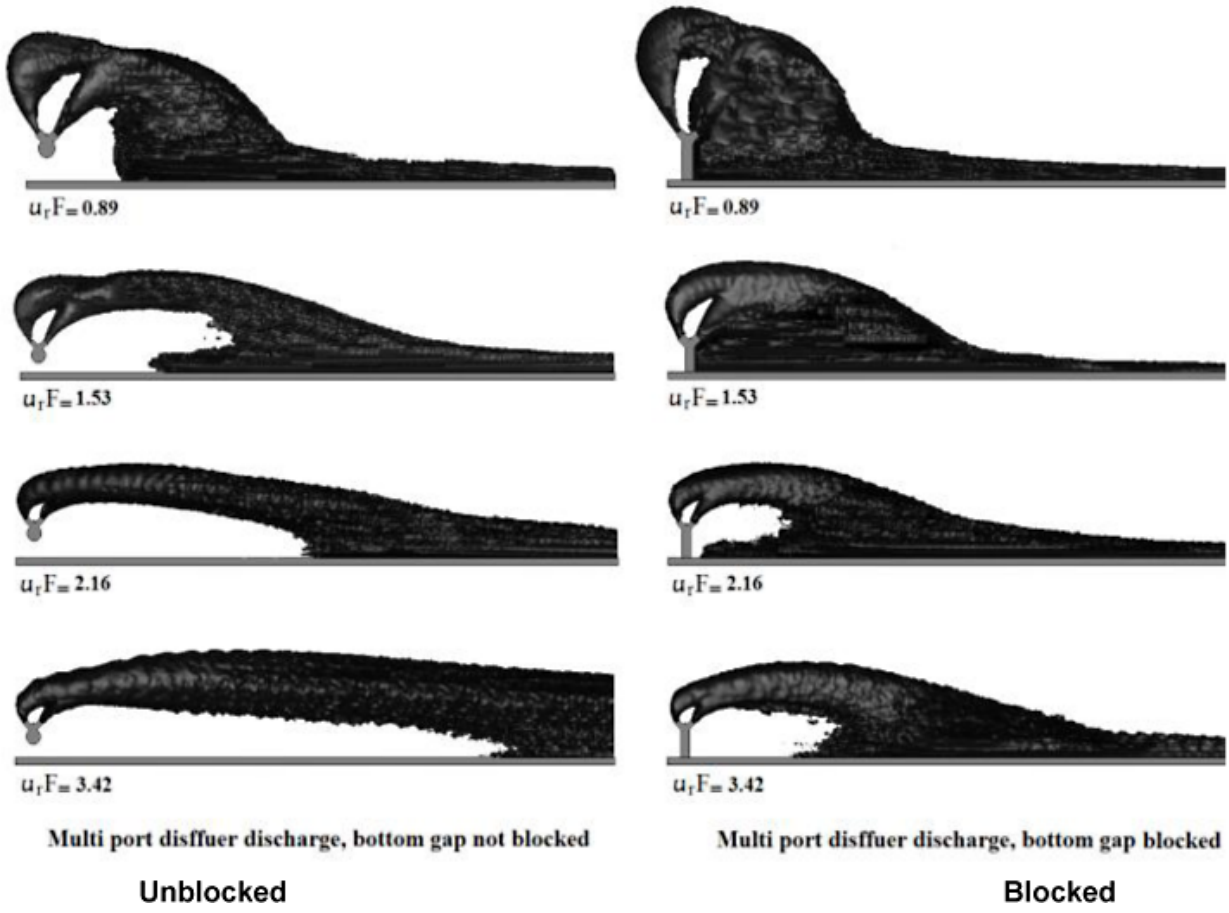

Figure 35. Effect of flow blocking.

The flow properties, as defined in Figure 36, were obtained: maximum rise height, location of impact point, and dilution at maximum rise height and impact point. The normalized results are plotted in Figures 37 to 39. Moreover, for these parameters, flow trajectory for different u_rF in both blocked and unblocked conditions was identified and then compared to each other.

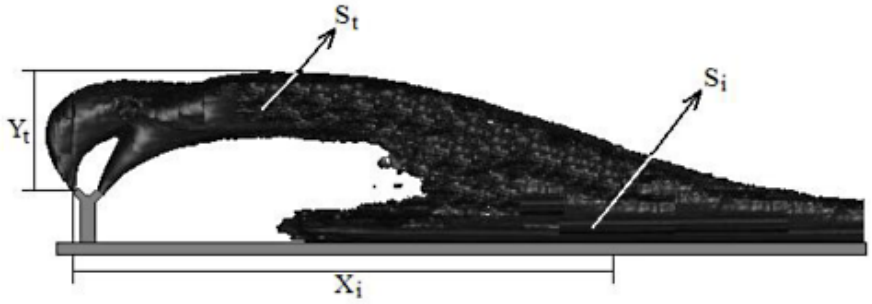

Figure 36. Schematic of major flow properties.

Unblocked flows

As shown in Figure 37, for flow maximum rise height, changes in y_t /dF were observed with increases in s/dF. In the 3D Tecplot flow visualizations, no merging was visually observed for those experiments with s/dF in the range of observation (s/dF = 0.9 to 6). So the variation of y_t with s/dF is unexplained.

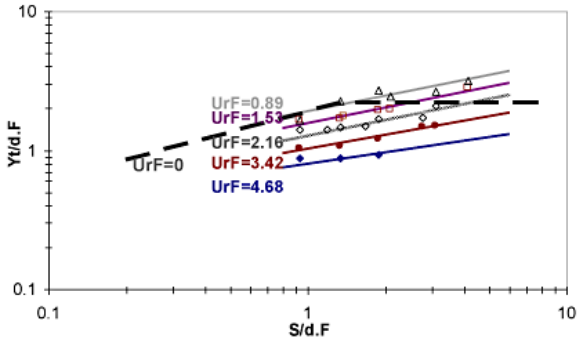

Figure 37. Variation in impact point location with *s/d*F for different u_rF – Unblocked diffuser.

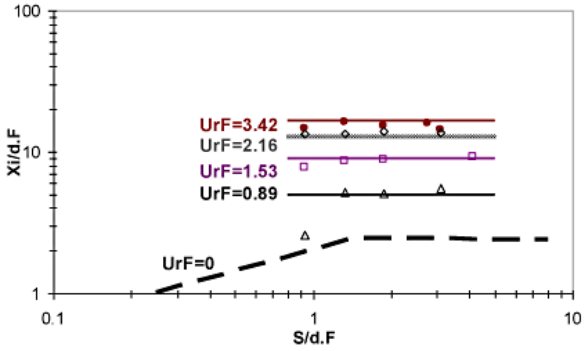

Figure 38. Variation of maximum rise height with *s/d*F for different u_rF – Unblocked diffuser.

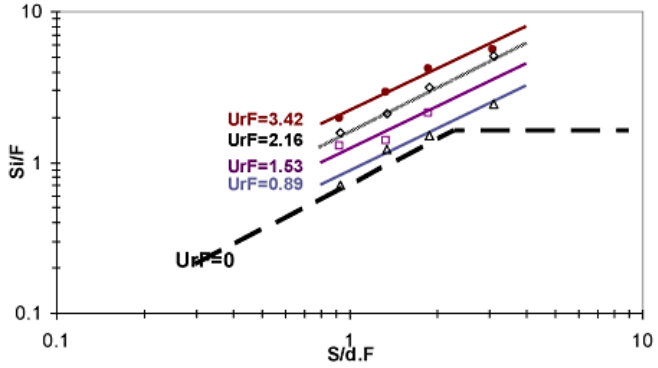

Figure 39. Variation in impact point dilution with *s/d*F for different u_rF – Unblocked diffuser.

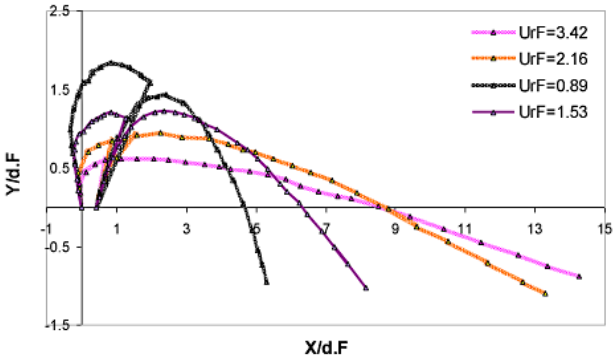

Figure 40. Trajectories for various u_rF, *s/d*F = 0.93 to 3.11 – Unblocked diffuser.

Blocked flows

Results for flows with blocking are shown in Figures 41 to 44.

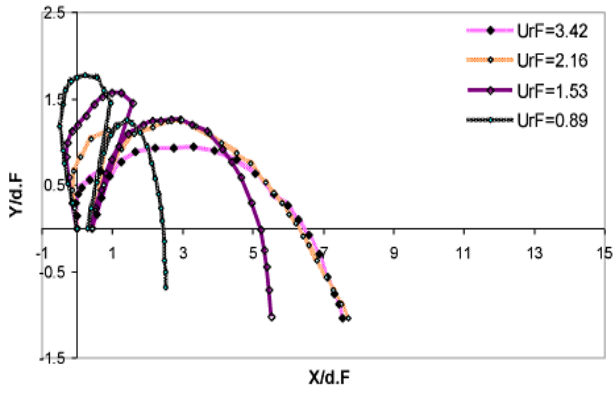

Figure 41. Trajectories for various u_rF in *s/d*F = 0.93 to 3.11 – Blocked diffuser.

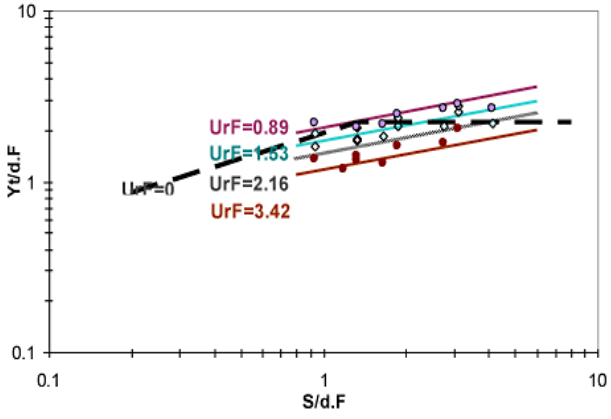

Figure 42. Maximum rise height for various *s/d*F for different u_rF – Blocked diffuser

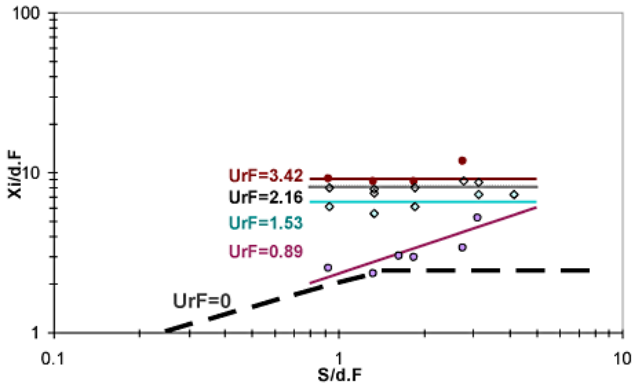

Figure 43. Location of impact point with *s/d*F for different u_rF – Blocked diffuser.

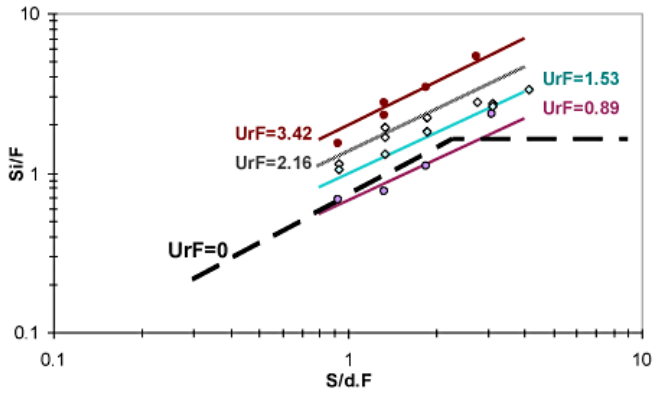

Figure 44. Impact point dilution for various *s/d*F for different u_rF – Blocked diffuser.

Comparisons of flow behavior of these two conditions show differences between flow properties for blocked and unblocked conditions. As shown in Figure 44, the impact point is farther downstream in the unblocked cases. Dilution at the impact point is higher in unblocked cases than in blocked cases (Figure 45).

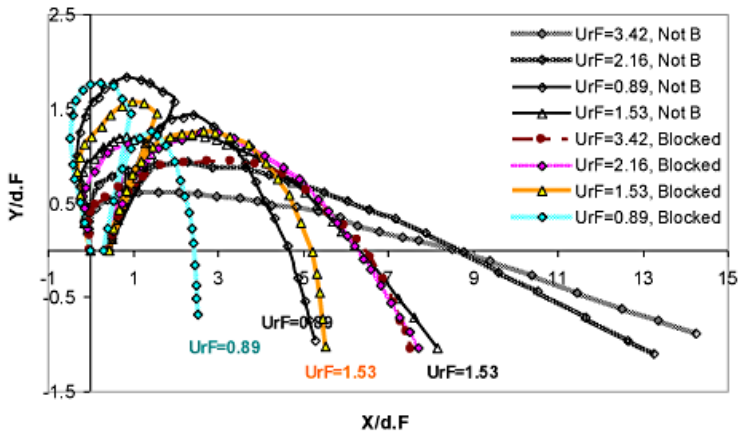

Figure 45. Trajectories for blocked and unblocked diffusers, *s/d*F = 0.93 to 3.11.

4.4.3 Discussion

From these experiments on two-sided diffusers, it can be concluded that:

The wastefield geometric characteristics and dilution depend on the ambient current speed (u_rF).

The maximum rise height depends on port spacing and Froude number. It increases when *s/d*F increases in the range of 0.9 to 4.1. Figure 42 shows that y_t for blocked condition is different from unblocked.

The impact location (x_i) in both blocked and not blocked cases do not show any dependence on *s/d*F. However, for the experiment with blocked condition the length of the impact point is apparently shorter than the unblocked cases. The impact point dilution also increases with increases in *s/d*F over the range of tested parameters and are not the same for blocked and unblocked cases.

The flow trajectories in blocked and unblocked cases show a significant influence of blocking on flow behavior. Blocking increases the maximum rise height and decreases the impact point length.

In blocked condition flow dilution at impact point is less than when unblocked. These results show how a small gap beneath diffuser can significantly impact the flow field and can increase mixing and dilution in flowing ambient waters.

4.5 Rosette Diffuser in Stagnant Ambient Water

4.5.1 Experiments

In this series of experiments, the behavior of flow discharged from rosette diffusers was tested with no ambient current. Two different riser configurations were used, each had four ports uniformly distributed around the riser perimeter (i.e., at 90° to each other in planform). Either the ports were oriented perpendicular and parallel to the diffuser axis (Figure 46), or at 45° to the diffuser axis (Figure 47). The experiments were conducted with either one or three risers for different spacing (s = 6.5 to 91 cm, 1 and 3 risers positioned at the width of tank). The conditions for the experiments are:

One riser with 0° orientation
Number of experiments: 9
F = 20.8 to 62.5
s/dF = 5.7 to 20.2

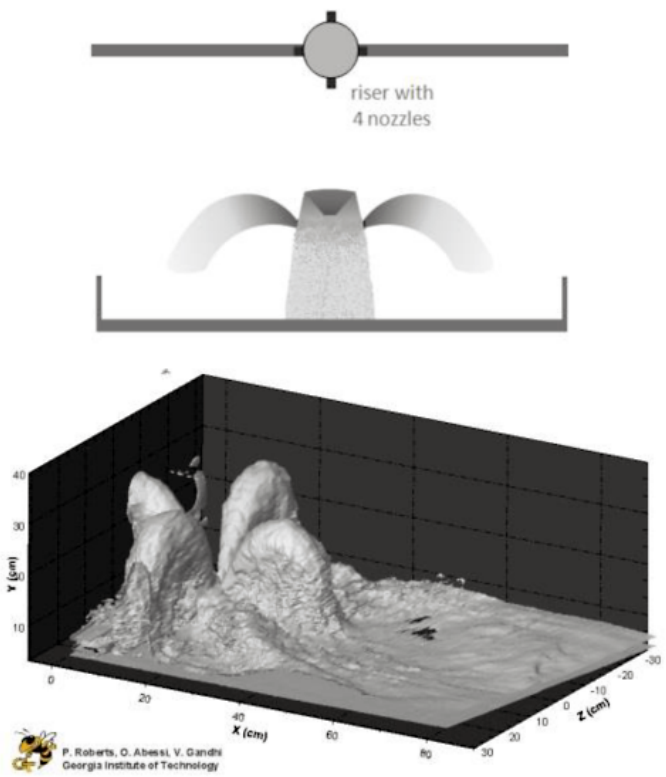

Figure 46. Flow from single rosette riser in 0° orientation.

One riser with 45° orientation
Number of experiments: 4
F = 29.2 to 62.5
s/dF = 6.7 to 15.9

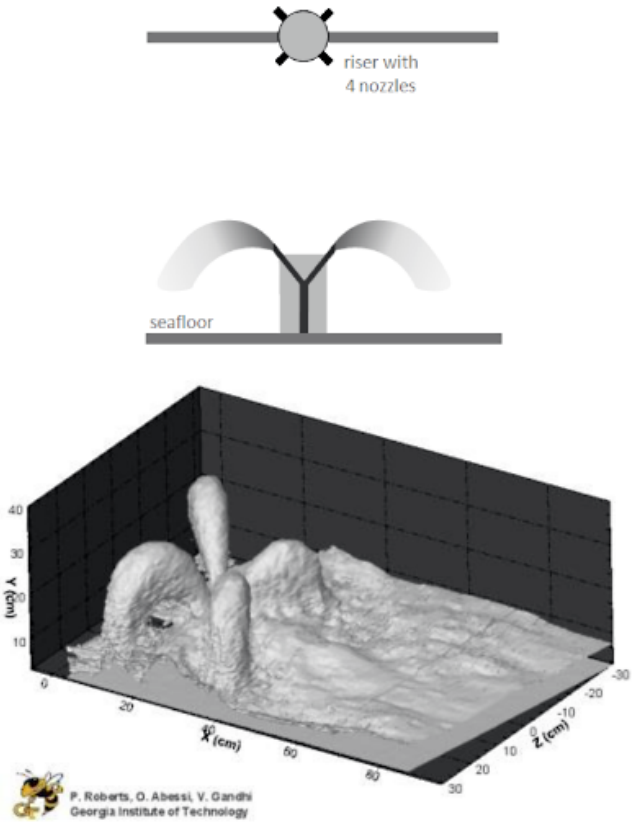

Figure 47. Flow from single riser in 45° orientation.

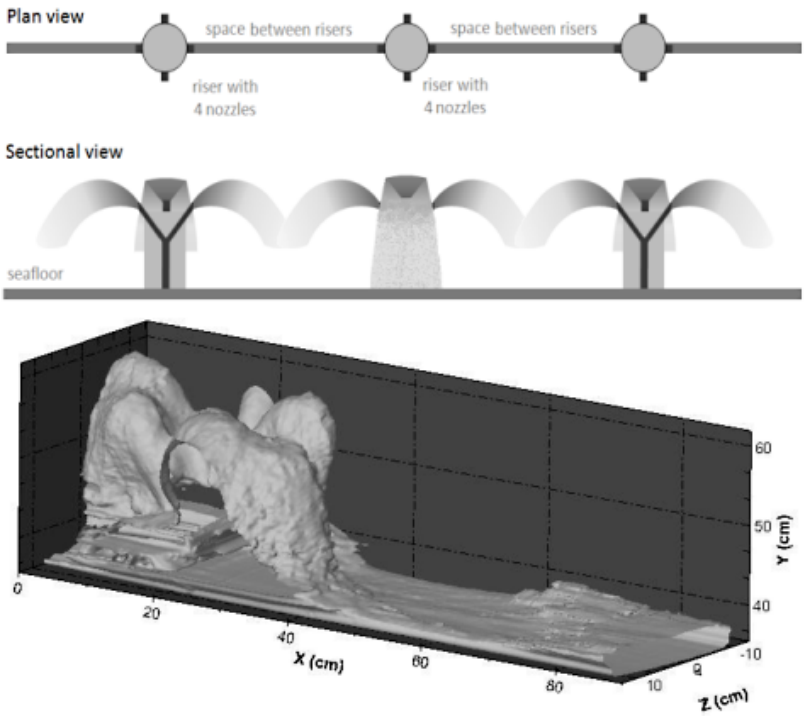

Three risers with 0° orientation
Number of experiments: 3
F = 41.7 to 66.7
*s/d*F = 0.36 to 0.58

Figure 48. Flow from three risers in 0° orientation.

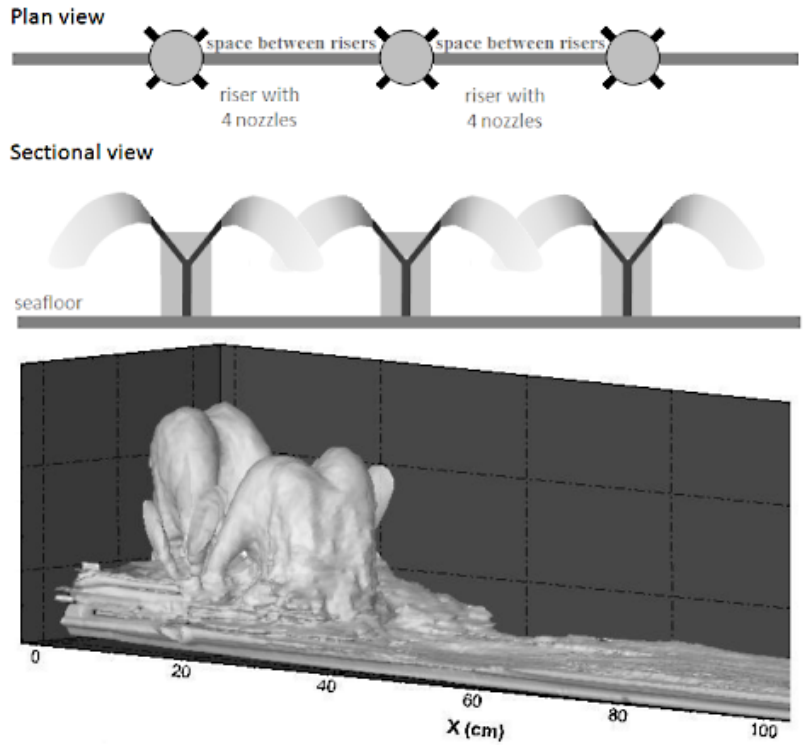

Three risers with 45° orientation
No. of experiments: 9
F = 25.0 to 58.4
*s/d*F = 0.51 to 2.08

Figure 49. Flow from three risers in 45° orientation.

In these experiments, as shown in Figure 50, three flow properties (geometric and mixing) such as dilution at the end of initial mixing zone (near field), location of near field, and waste field thickness at the end of the near field were investigated for different riser spacing.

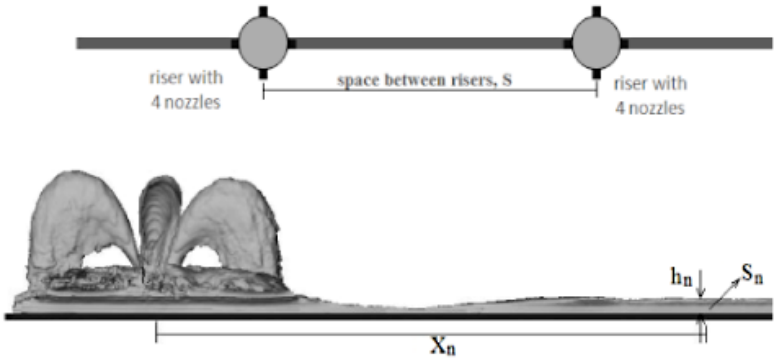

Figure 50. Riser configuration flow properties.

The properties are plotted in dimensionless form in Figures 51 to 53.

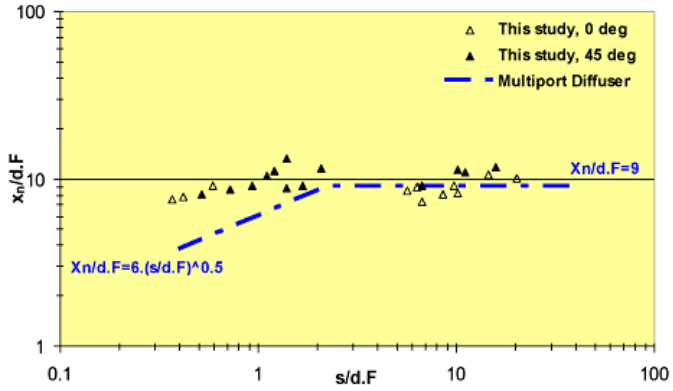

Figure 51. Location of near field.

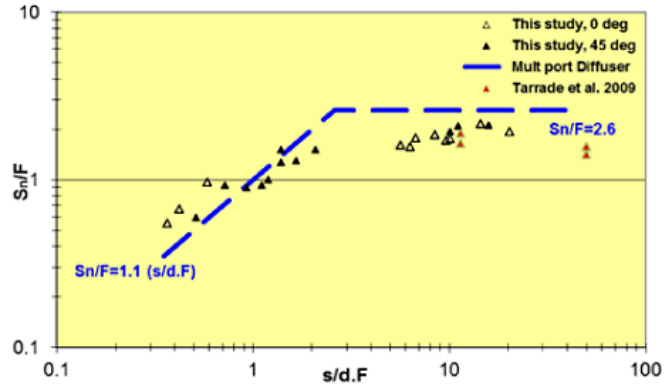

Figure 52. Dilution at the end of near field.

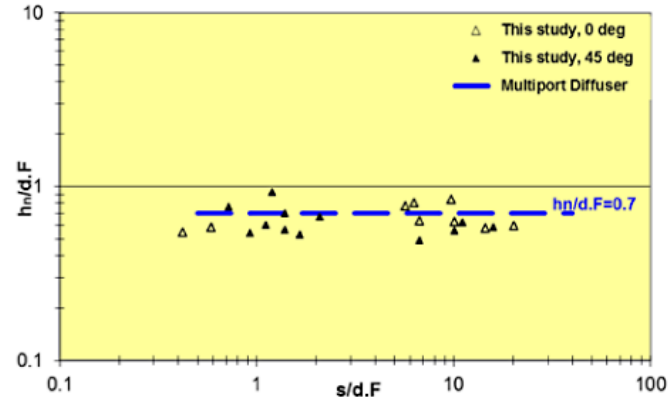

Figure 53. Wastefield thickness at the end of the near field.

4.5.2 Discussion

From these experiments it can be concluded that: For the experiments with one and three risers, the difference in dilution and location of the near field for the 0° and 45° rosette orientation configurations is negligible. The near field location and the dilution there depends on riser spacing for small spacing ($s/d\mathsf{F} < \sim 2.5$), but becomes independent of spacing for $s/d\mathsf{F} > \sim 3$.

The slope of the best-fit lines to the data in the region where merging occurs is different for dilution than for near field length. The dilution line is steeper, indicating greater sensitivity to spacing for dilution. The wastefield thickness at the end of the near field shows little dependence on riser spacing over the range tested.

Comparison of near field flow properties for the rosette and multiport diffusers shows that the dilution for rosettes are generally lower for large spacing but similar for smaller spacing. This is true for both line and point source conditions. This may be because of merging on the lower boundary for the rosettes.

4.6 Rosette Diffuser in Flowing Ambient Currents

4.6.1 Experiments

In this series of experiments, the behavior of flow discharged from rosette diffusers in the two riser orientations, 0° and 45°, for different spacing (s = 6.5 - 91 cm) for one and three risers is investigated. The experimental conditions are:

One riser with 0° orientation
Number of experiments: 8
F = 41.7, 62.5, 83.3
$s/d\mathsf{F}$ = 5.05, 6.74,10.1
$u_r\mathsf{F}$ = 1.02 to 3.88

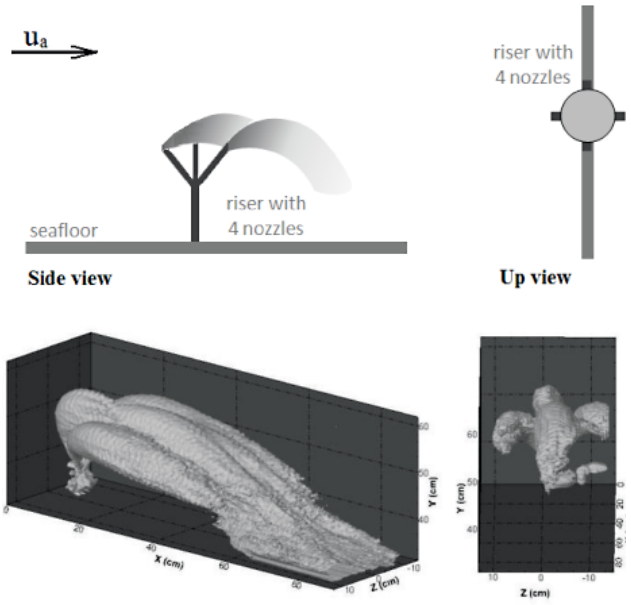

Figure 55. Flow configuration for rosette diffuser in flowing water with 45° orientation.

One riser with 45° orientation
Number of experiments: 16
F = 29.2 to 83.3
$s/d\mathsf{F}$ = 5.05 to 14.4
$u_r\mathsf{F}$ = 1.02 to 3.88

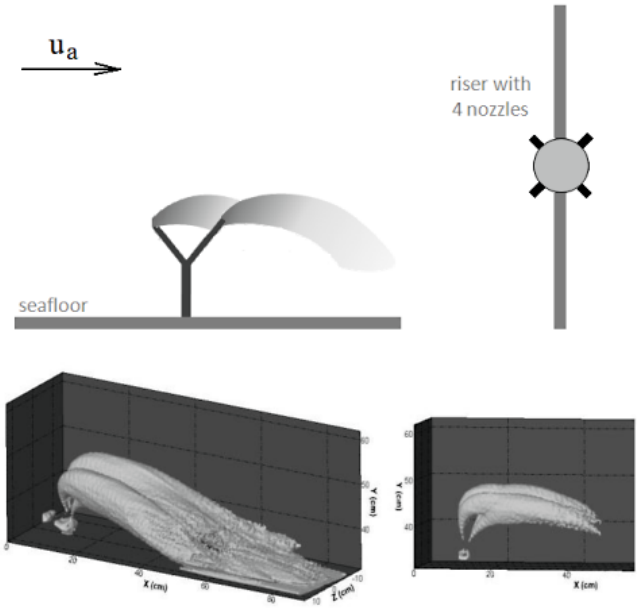

Figure 54. Flow configuration for rosette diffusers in flowing water - 0° orientation.

Three risers with 45° orientation
Number of experiments: 9
F = 25 to 58.6
s/dF = 0.51 to 1.38
u_rF = 1.02 to 3.88

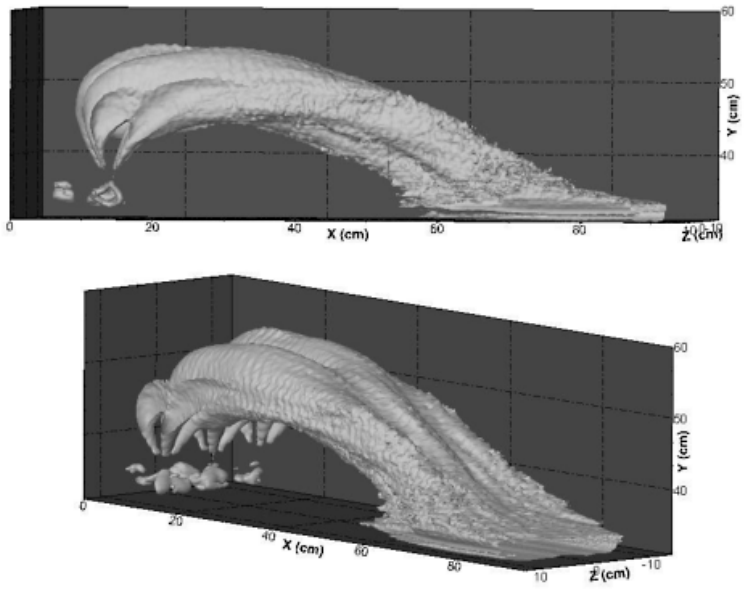

Figure 56. Flow configuration for 3 rosette diffuser with 45° orientation.

In the second and third series of experiments, as shown in Figure 57, three parameters: discharge maximum rise height, location of impact point, and dilution at the impact point were investigated. The parameters were then normalized and plotted for different u_rF against s/dF. The results are plotted in Figures 58 to 60.

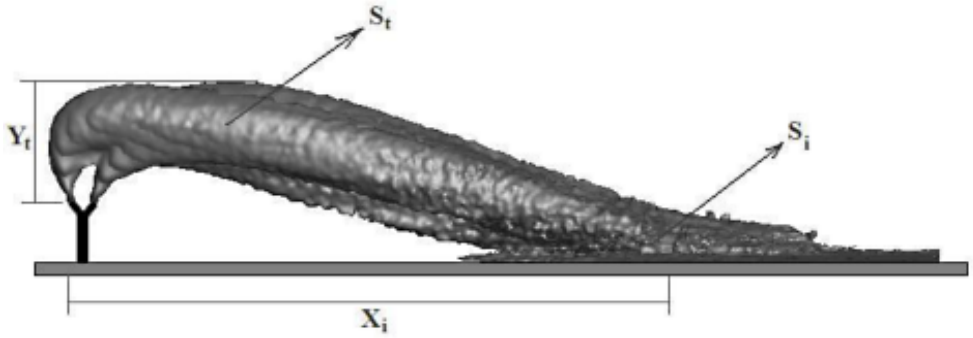

Figure 57. Flow configuration and parameters of flow geometry and mixing.

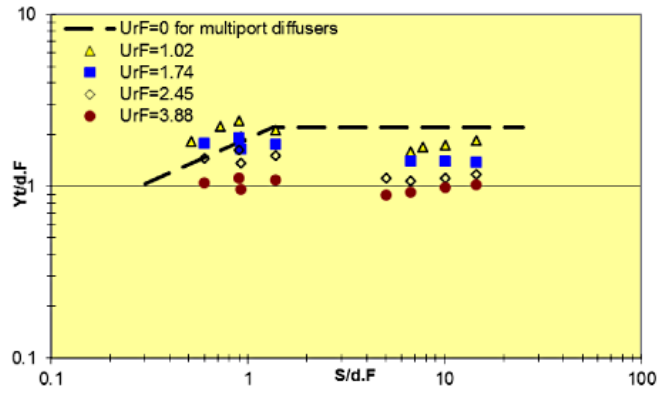

Figure 58. Maximum rise height for rosette diffuser for different u_rF, 45° orientation.

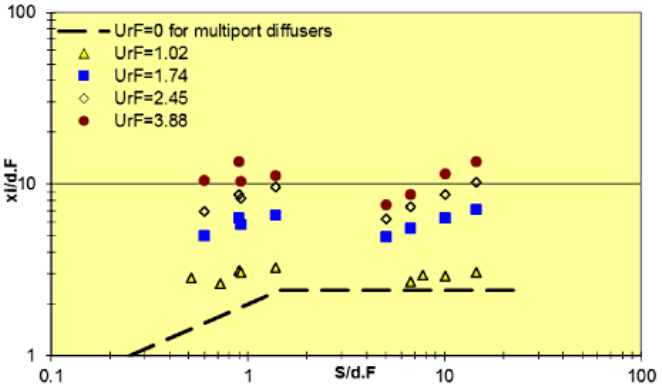

Figure 59. Impact point location for rosette diffuser for various u_rF.

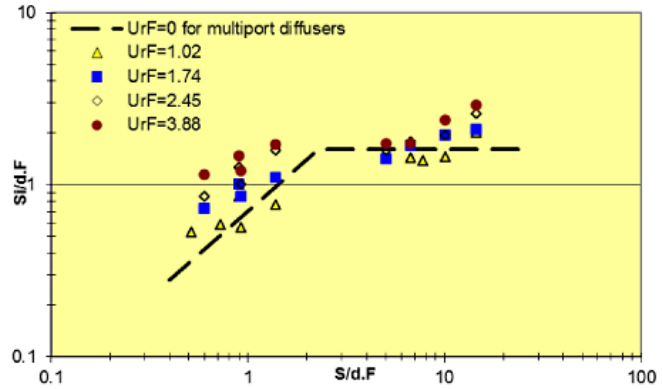

Figure 60. Dilution at impact point in rosette shape diffuser for various u_rF.

In addition to these parameters, jet trajectories for various conditions were also investigated. Because the flow from rosette diffusers is three dimensional, the geometries in the 3D experiments were normalized by dividing by dF and plotted for different ambient current speeds (different u_rF) in Figures 61 through 68. As can be seen, increases in ambient current velocity (u_rF) cause the flow to deflect farther from the source and impact the bottom farther away. As shown in Figure 60, dilution at the impact point location also increases when u_rF increases.

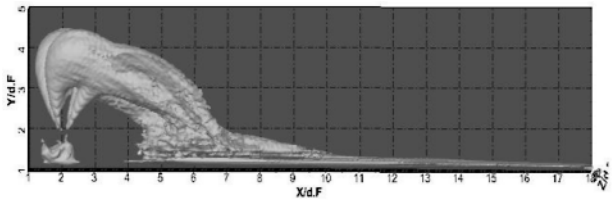

Figure 61. Rosette discharge, u_rF = 1.02, s/dF = 10.11, Exp14, 16 Apr 2012

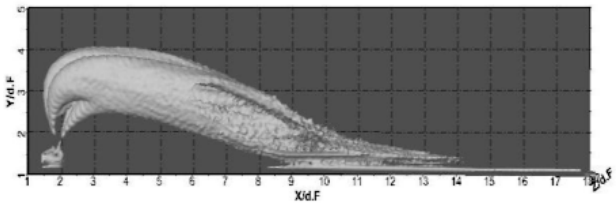

Figure 62. Rosette discharge, u_rF = 1.74, s/dF = 10.11, Exp11, 16 Apr 2012.

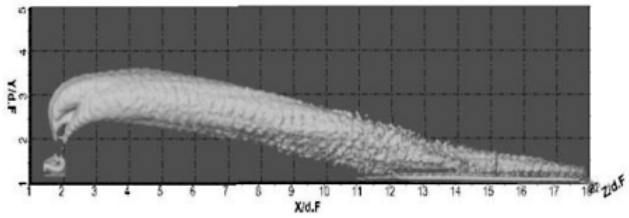

Figure 63. Rosette discharge, u_rF = 2.45, s/dF = 10.11, Exp1, 16 Apr 2012.

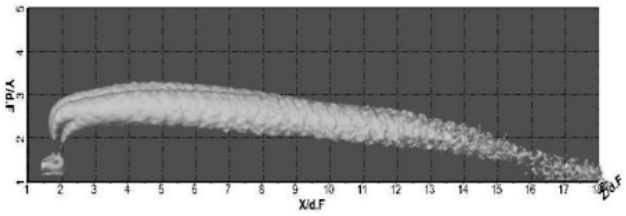

Figure 64. Rosette discharge, u_rF = 3.88, s/dF = 10.11, Exp7, 16 Apr 2012.

In Figures 65 through 72, flow trajectories for three closely spaced risers distributed across along the width of tank are shown. Due to the narrow spacing, the discharged flows merge, changing the flow trajectories and reducing mixing and dilution.

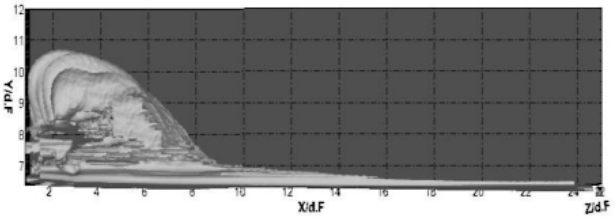

Figure 65. Three rosette risers, u_rF = 1.02, s/dF = 1.38, Exp2, 20 Apr 2012.

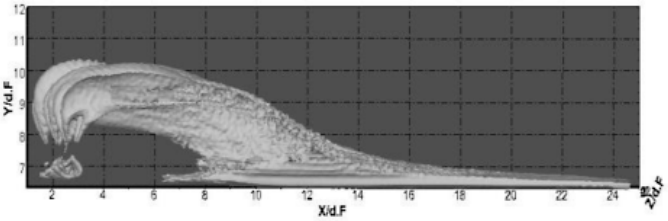

Figure 66. Three rosette risers, u_rF = 1.74, s/dF = 1.38, Exp8, 19 Apr 2012.

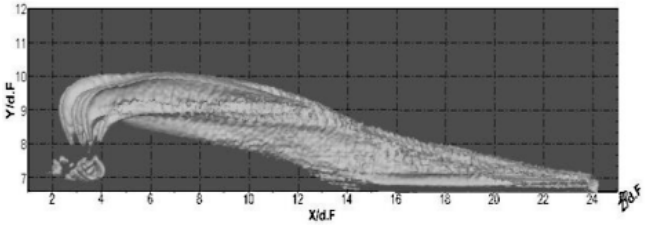

Figure 67. Three rosette risers, u_rF = 2.45, s/dF = 1.38, Exp4, 19 Apr 2012.

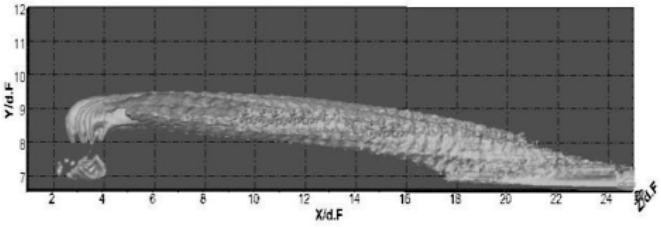

Figure 68. Three rosette risers, u_rF = 3.88, s/dF = 1.38, Exp6, 19 Apr 2012.

As previously discussed, some experiments with another configuration of discharge, 0° orientation toward downstream, were also conducted with only one riser. A few experiments were conducted in this case and like before flow maximum rise height, the location of impact point and flow dilution at impact point were identified. The results are shown in Figures 70 through 72.

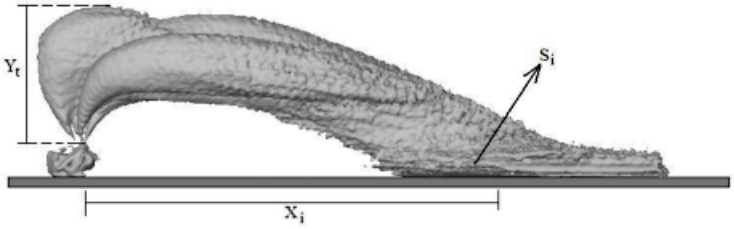

Figure 69. Main flow properties for 0° orientation.

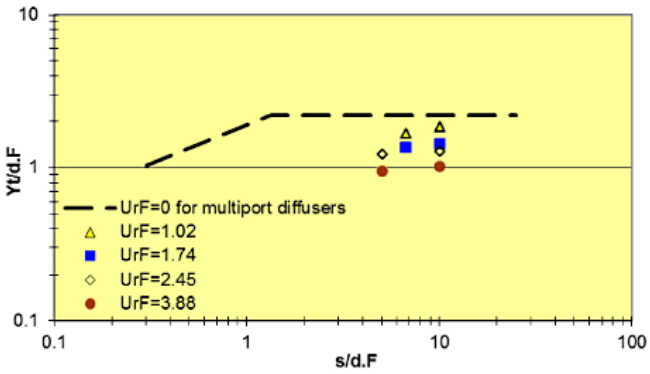

Figure 70. Maximum rise height in rosette shape diffuser for different u_rF, 0° orientation.

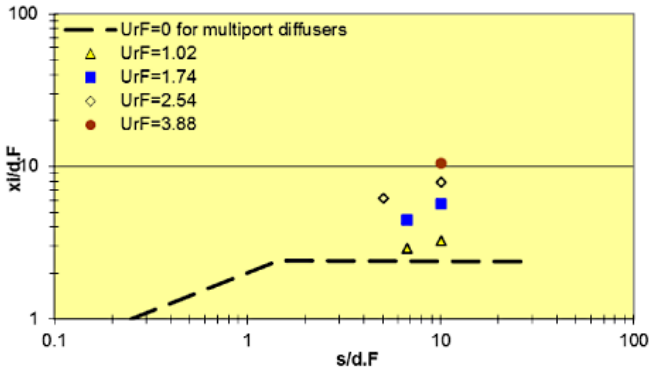

Figure 71. Impact point location for rosette diffuser for different u_rF, 0°

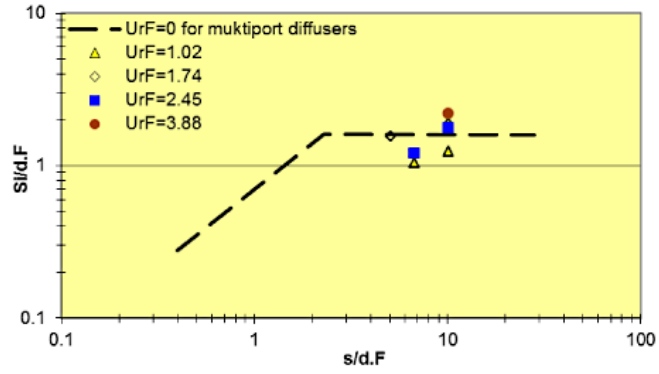

Figure 72. Dilution at impact point for rosette diffuser for different u_rF, 0° orientation.

To show the changes in flow trajectory for different conditions in the ambient current, the flow 3D experiments were normalized by dividing by dF and shown for different u_rF as had been done in previous experiments. Figures 73 through 76 clearly show the changes in flow behavior and the location of impact point with changes in u_rF.

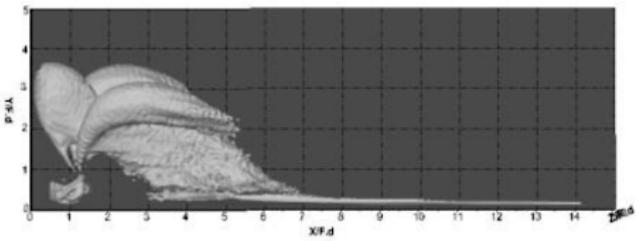

Figure 73. Flow configuration for one riser with u_rF = 1.02, s/dF = 10.11, Exp11, 17Apr 2012.

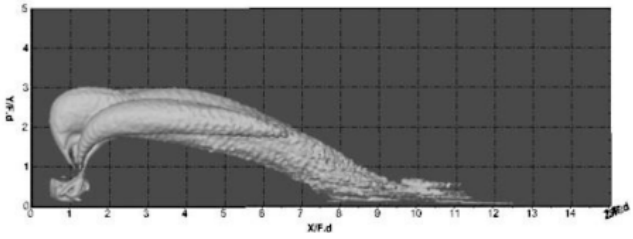

Figure 74. Flow configuration for one riser with u_rF = 1.74, s/dF = 10.11, Exp9, 17Apr 2012.

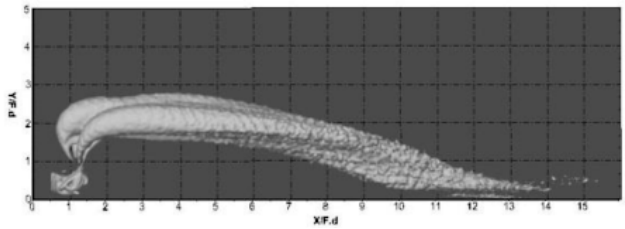

Figure 75. Flow configuration for one riser with u_rF = 2.45, s/dF =10.11, Exp8, 17Apr 2012

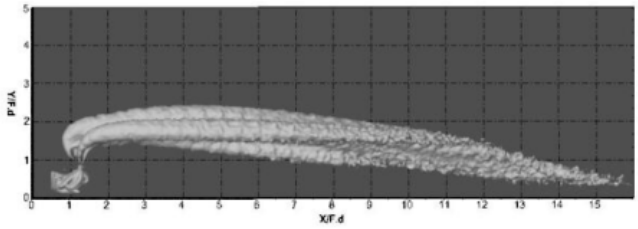

Figure 76. Flow configuration for one riser with u_rF = 3.88, s/dF = 10.11, Exp6, 17Apr 2012.

4.6.2 Influence of Riser Configuration

For the discharge from the rosette diffuser in flowing ambient water, as previously discussed, two configurations of discharge, 0° and 45° orientation, were investigated. The results show that, like the stagnant condition, in a flowing current, the configuration does not significantly affect the flow and riser orientation can be considered of secondary importance. Figures 77 through 79 show the maximum rise height, location of impact point, and dilution at the impact point for 0°45° orientations. The figures show only slight changes of flow characteristics for the different orientations.

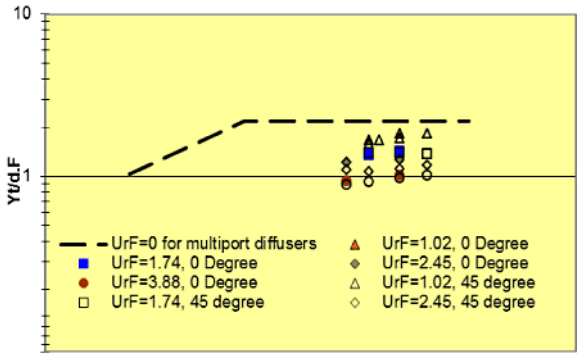

Figure 77. Comparison of flow maximum rise height for 0° and 45° orientations in flowing currents.

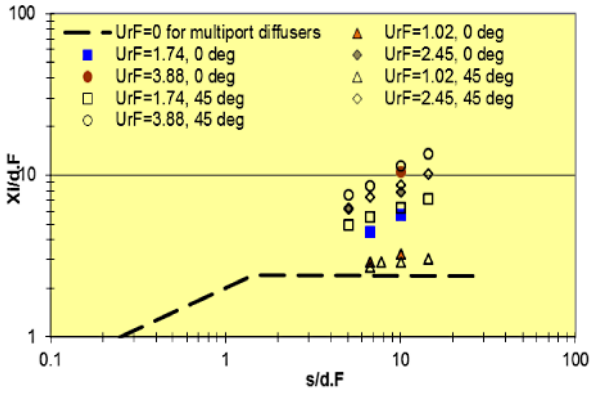

Figure 78. Comparison of flow impact point for 0° and 45° orientations in flowing currents.

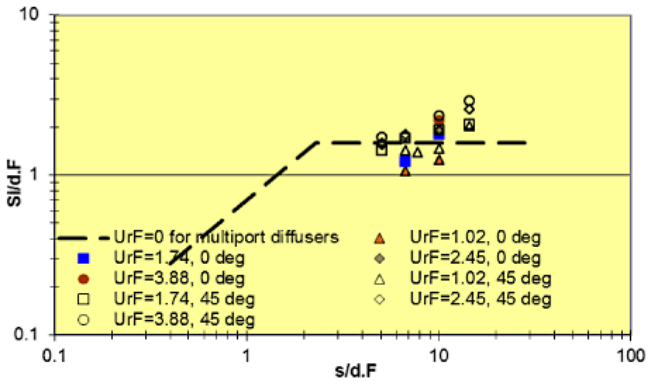

Figure 79. Comparison of flow dilution at impact point for 0° and 45° orientations in flowing currents.

4.6.3 Discussion

From these experiments on the flow from rosette diffusers in flowing currents, the following flow properties were obtained: maximum rise height, location of impact point, dilution of flow at impact point, and the 3D flow trajectories for various u_rF. The results were plotted in normalized form from which it can be concluded that:

For large riser spacing, the results do not show constant values like those previously observed in co-flowing water.

For the smaller spacing where jet merging influences the flow behavior, the maximum rise height and impact point location exhibited a different behavior. These parameters increased compared to larger spacing, which means that, different from diffuser discharge, y_t and x_i increase after merging; merging and the Coanda effect are not influential to decrease y_t and x_i.

Flow normalized trajectories for various u_rF show the high importance of ambient current on the flow behavior and show how increases in ambient cross flow increase the length of impact point and dilution at this point. The influence of nozzle orientation is of secondary importance and can be ignored.

4.7 Effect of Nozzle Inclination

4.7.1 Experiments

The optimum nozzle angle for dense discharges has been the subject of some controversy. In this series of experiments, the influences of discharge angle for single jets discharging into stagnant environments are investigated. Jet terminal rise height (up to 10% of C_m), y_t, centerline maximum height, y_m, the location of maximum height, xt, dilution at this point, S_t, the location of impact point, xi, impact point dilution, S_i, location of near field, x_n, and near field dilution S_n (defined in Figure 80) were identified and compared with other studies and predictions of numerical models. The main goal of this study, besides comparing flow properties for different angles, is to find the optimal diffuser design.

A total of 49 experiments, two- and three-dimensional, were done for nozzle angles ranging from 15° to 85°. The experimental conditions are summarized in Table A2.

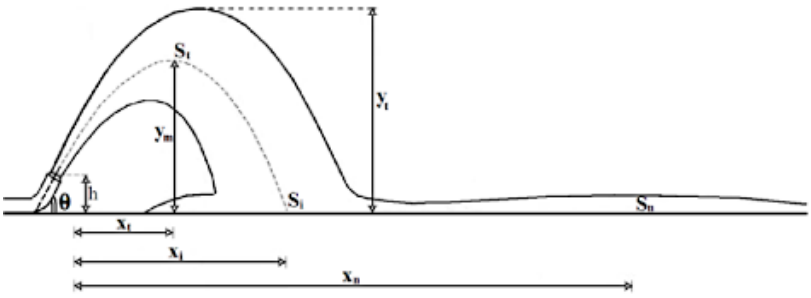

Figure 80. Configuration for single port dense jets.

4.7.2 Results

Flow properties were normalized by the buoyant jet length scale (L_M) and then plotted against nozzle angle. The results were compared with data previously published in the literature and the predictions of numerical models.

A typical time-averaged three-dimensional flow visualization for a 45° inclined dense jet is shown in Figure 81. The outer surface is shown as a semi-transparent gray iso-concentration surface, whose level is approximately 10% of the maximum centerline concentration. Also shown in Figure 81 is the two dimensional concentration field (with concentration levels shown in false color) extracted from the centerline longitudinal plane of the three-dimensional files.

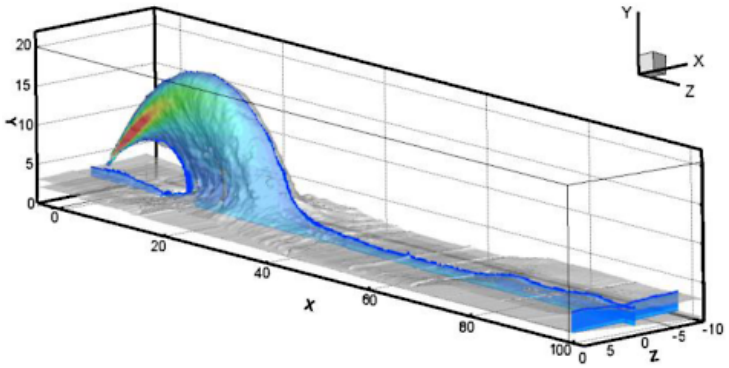

Figure 81. A typical time-averaged three dimensional flow visualization for a 45° jet.

Central planar tracer fields for all nozzle angles are shown in Figure 82. The planes are vertical and parallel to the jet direction and pass through the nozzle centerline (*x*-*y* plane). The tracer concentration levels are shown in false-color contours and distances are normalized by L_M.

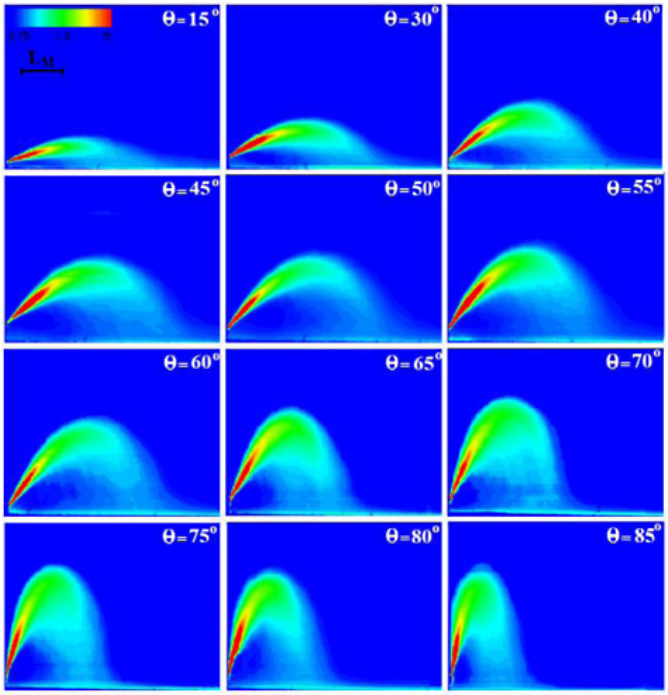

Figure 82. Central plane tracer concentrations for various nozzle angles.

Figure 82 shows that the normalized jet trajectories are mainly affected by the jet discharge angle. As the angle increases, the terminal rise height increases to a maximum at around 70° and then becomes essentially constant. Beyond about 70°, the rise height is limited by re-entrainment of the falling plume into the rising jet. The horizontal location of the impact point increases to a maximum around 45°, then decreases for steeper angles. Jet entrainment begins immediately near the nozzle and dilutes the flow up to the maximum height. After this point, however, the flow converts to a more plume-like flow with some detrainment in the lower part. The detrainment destroys the axi-symmetry of the dense jets; this is known as gravitational instability and was reported by Kikkert et al. (2007), Shao and Law (2011), and Lai and Lee (2012). The descending flow then impacts the floor and starts to spread radially outward. Vortices cause further entrainment but collapse at some distance from the impact point, leaving flow stably stratified with undulating internal waves. So, beyond the impact point further mixing and dilution occurs up to where the turbulence and vortices collapse, marking the end of the near field. The dilution at this point is important in the design and construction of dense discharges as no further dilution occurs due to near field processes. For further discussion of the definition of the near field and the mechanism of turbulence collapse see Roberts et al. (1997).

Profiles of mean concentration along the jet trajectories are not symmetrical. For the rising phase the profiles are well-approximated by Gaussian distributions for all nozzle angles. Near the maximum height, the lower half of the jet begins to depart from Gaussian whereas the upper half is still Gaussian, and in the descending phase the profiles deviate further from Gaussian due to the buoyancy-instability. At the maximum height the profiles become more asymmetric as the nozzle angle increases up to 85°. In the descending phase, the asymmetry is most pronounced for angles less than about 60° but decreases for steeper angles.

The upper half of the jet is always (half) Gaussian while the lower part, due to detrainment that begins near to the source, becomes increasingly non-Gaussian farther downstream. These changes in the cross sectional profiles were recently discussed by Lai and Lee (2012). They concluded that the concentration profile stabilized beyond the maximum rise and did not become more distorted. The present experiments showed, however, that for smaller angles, the distortions become more pronounced beyond the maximum rise height while they are about the same for 45° to 60° jets. For 75° to 85°, the distortions decrease and the concentration profiles becomes more symmetric.

The major geometrical and mixing parameters (defined in Figure 80) for different angles were extracted from the 2D time-average concentration fields using the methods discussed above and are summarized in Table A2. The results are plotted in dimensionless form as functions of nozzle angle in Figures 83 through 86 along with previous data. Note that in other studies the parameters may be defined differently by different investigators. In the present study, to better simulate actual brine diffusers, the nozzle was elevated above the floor ($h/d \approx 3.2$ to 7.8) and rise heights were measured from the nozzle tip. The horizontal locations of the impact point and the near field were defined from the nozzle tip. The terminal rise was defined as where the concentration was 10% of the transverse maximum concentration at the location of jet maximum height.

Figure 83 shows the terminal rise height y_t. It gradually increases as the discharge angle increases up to 75° and then becomes essentially constant. Differences between the present results and previous experiments could be due to fact that the jet boundary is defined differently. Lai and Lee (2012), Shao and Law (2010) and others define it as the locus of 25% of the local maximum concentration, cm (which they assumed to be the visual boundary) while 10% of c_m is used here. Lai and Lee also defined the terminal rise height as the vertical distance from the nozzle tip, whereas here they are measured from the floor. The maximum value of the terminal rise height yt/ $L_M \approx 3$ occurs for 75° and larger angles, and can be used as a design criterion for shallow water to avoid jet impingement with the free surface which is assumed to influence jet mixing and dilution (Jiang et al. 2012).

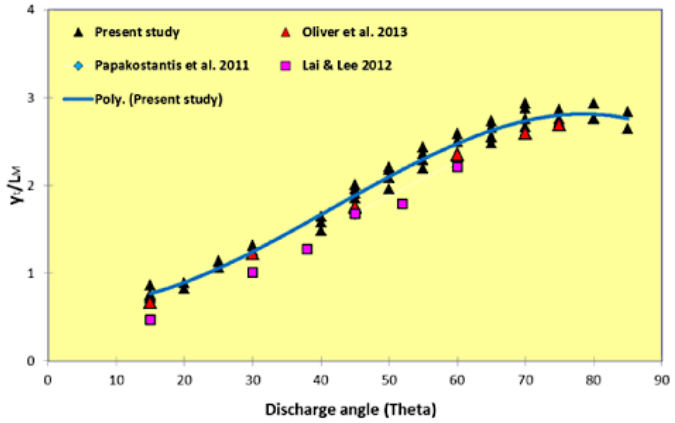

Figure 83. Terminal rise height for various nozzle angles.

The horizontal location of the impact point is plotted in Figure 84. Good agreement is observed between the present and previous experiments. The jet reaches its longest trajectory for the range of 40° to 45°.

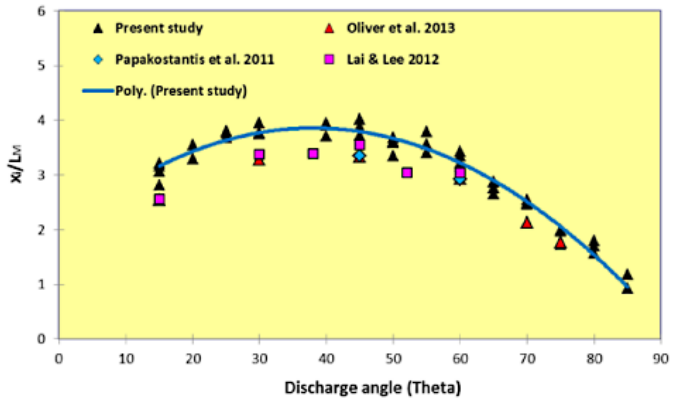

Figure 84. Location of impact point for various nozzle angles.

Figure 85 shows the measured minimum dilution at the impact point (Si). This is an important parameter in design because this is the first point of brine contact with sea bed organisms and corresponds to the lowest seabed dilution. Figure 85 shows the dilution to be essentially constant for nozzle angles 45° to 65° which makes it challenging to find the optimal angle by experimentation. This is further addressed by the use of computational models in the following section.

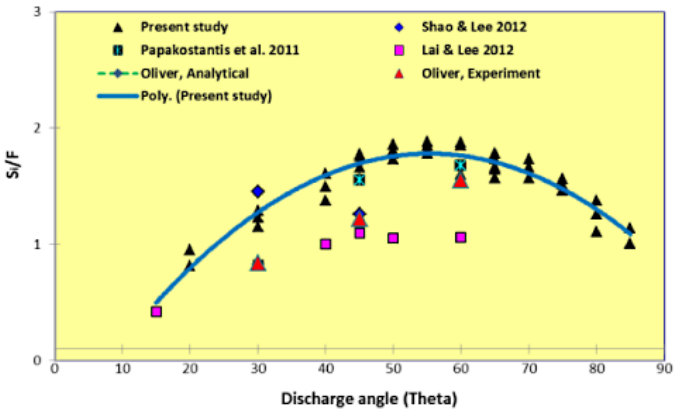

Figure 85. Impact point dilution for various nozzle angles.

Since Zeitoun et al. (1972) suggested that 60° jets have the longest trajectory and highest dilution, this angle has been generally accepted as the optimal. Additional dilution was reported by Roberts et al. (1997) for 60° jets beyond the jet impact point due to entrainment and turbulence in the spreading layer. The location where the turbulence and vortices collapse was suggested as the end of near field where water quality standards must be met.

Figure 86 shows the near field dilution for various discharge angles. The near field is defined as the location where no more dilution occurs downstream near the bed. The experimental values reported by Roberts et al. for 60° jets are also plotted; no more data have been found for near field dilution. Figure 86 shows greater sensitivity of dilution. The highest dilution occurs for 50° to 60°, so 55° may be a good approximation for optimal design to maximize near field dilution. The near field dilution is about 10 to 35% higher than the impact point dilution and this increase varies with nozzle angle. For smaller angles, less than 30°, the increase in dilution is about 10 to 20%, for 35° to 65° it is about 25 to 35% and then it decreases again down to 10 to 15% for 70° to 85°. This is consistent with Roberts et al. (1997) estimates

of a 40% increase for 60° jets. This variation in dilution increase in the near field causes the near field dilution to be more sensitive to nozzle angle than the impact point dilution.

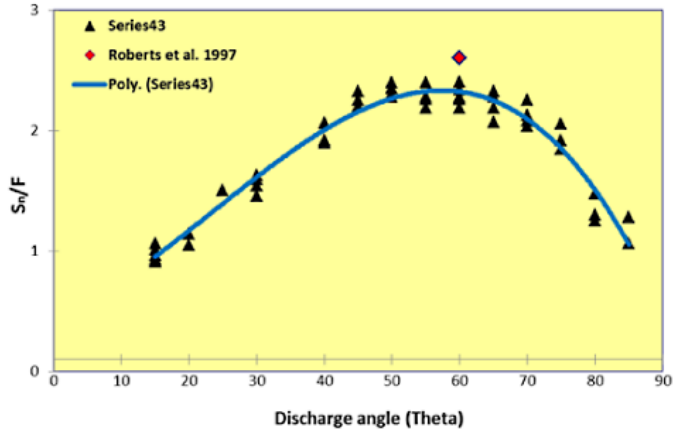

Figure 86. Near field dilution for various nozzle angles.

4.7.3 Computational models

Numerical models are commonly used to investigate flow properties in brine discharges. CORJET, JETLAG, and UM_3 are well-known computational models used for dense discharge modeling. These models are used in software packages CORMIX, VISJET, and VISUAL PLUMES, respectively. They have been widely applied to predict the behavior of brine discharges. These models are integral models based on the integration of differential conservation equations over the jet cross section. Changes in volume flux along the trajectory are predicted by an entrainment approach. The profiles are assumed to be always radially symmetric. CORJET uses an Eulerian approach and JETLAG and UM_3 a Lagrangian approach. Integration of the equations requires assuming an unlimited receiving water body, and consequently boundary effects, re-entrainment, and detrainment are not simulated in these models. Therefore, their results are only valid along the jet trajectory prior to bottom impact and do not extend in to and up to the end of the near field. The models are described in Palomar et al. (2012a) where the characteristics of each are explained in detail. Palomar et al. (2012b) also discussed the main features of the models applicable to dense jet modeling and ran them to simulate 30°, 45°, and 60° inclined jets. They compared the results of the numerical models with each other and with previous experimental data for stagnant environments and flowing current.

This section is focused on the computational model results and compares them with the present experimental results in order to better define the optimal design for each jet parameter. Results for JETLAG and CORJET that were previously reported in the literature are used. UM_3 was run for typical discharge conditions with four different aspiration coefficients (α) with the nozzle elevated $h/d = 6.3$ from the floor. The aspiration coefficient in UM_3 specifies the rate at which ambient fluid is entrained. Larger values cause more rapid mixing while lower values decrease mixing and dilution. The value of the aspiration coefficient also affects the geometrical characteristics such as the jet trajectory. The default value recommended by the model is 0.1 ($\alpha = 0.1$) but it can be changed by the user.

Figure 87 shows model predictions and our experimental results for terminal rise height. The experimental results and CORJET and JETLAG simulations indicate that the terminal rise heights increase with nozzle angle up to about 75° and then become approximately constant but both models significantly underestimate rise height. UM_3 results are shown for two aspiration coefficients, $\alpha = 0.1$

(default value) and 0.05. UM_3 also underestimates rise height for default but its predictions become much closer for smaller $\alpha \approx 0.05$. Similar trends were observed in other variables as discussed below.

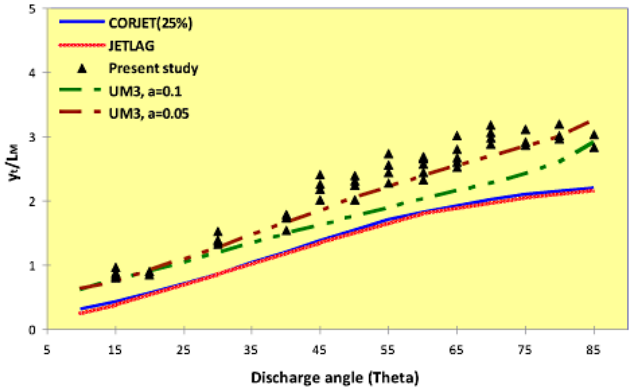

Figure 87. Terminal rise height for various nozzle angles and comparison with numerical results.

Figure 88 shows the impact location. CORJET, JETLAG, and UM_3 (for $\alpha = 0.1$) significantly underestimate the locations while for smaller alpha valves results are closer to the experiments. This figure implies that the maximum distance of impact occurs at 40° which is associated with the longest flow trajectory.

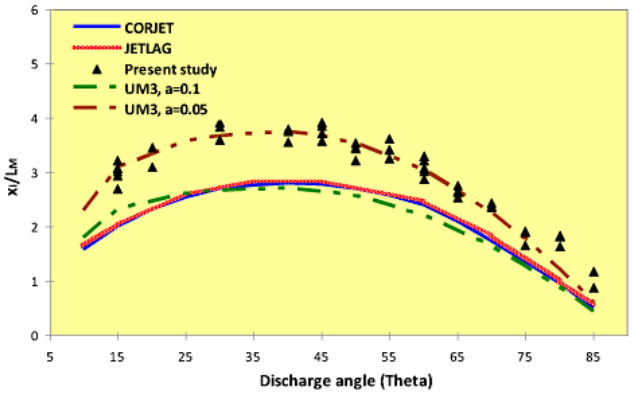

Figure 88. Location of impact point for various nozzle angles and comparisons with numerical results.

Figure 89 shows impact point dilution. Again, it shows that UM_3 with default predicts dilution better than CORJET and JETLAG. All models show an increase in dilution up to about 40° and little increase beyond. The numerical results imply that 50° is the optimum discharge angle for impact dilution, although there is little variation over the range from 40° to 70°.

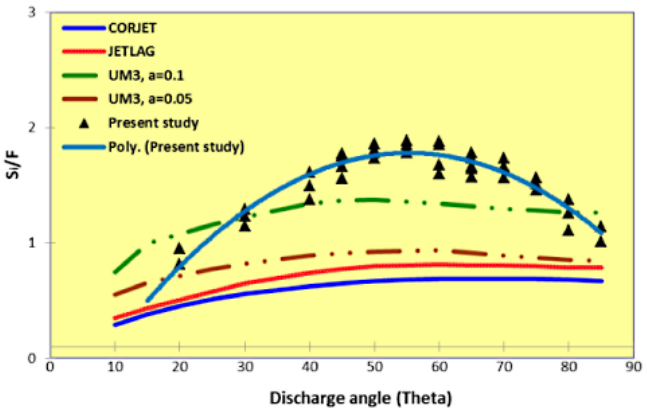

Figure 89. Impact point dilution for various nozzle angles and comparison with numerical results.

All of the models significantly underestimate geometrical properties, including UM_3 with the default aspiration coefficient, $a = 0.1$. Changing the aspiration coefficient in UM_3 to 0.05 improved its predictions considerably. JETLAG and CORJET significantly underestimated dilutions, but UM_3 predicted them quite closely with the default aspiration coefficient. Changing the aspiration coefficient in UM_3 to 0.05 resulted in considerably underestimating the dilution. It appears to be difficult to simultaneously predict flow geometry and dilution.

Integral models assume an unlimited environment and axisymmetric (round) profiles. The cross sectional profiles are also assumed to be self-similar and are Gaussian for CORJET and Top-hat for UM_3 and JETLAG. The models track the evolution of the average properties of a plume element along the trajectory. But the centerline is substantially less diluted than the average plume element. Centerline properties are calculated from the Top-hat averaged values assuming a tracer concentration profile over the cross-section. UM_3 uses a 3/2-power profile while JETLAG uses a Gaussian profile. The models integrate the profiles in cross section and then back fit them to calculate the peak-to-mean ratio between centerline and averaged values.

The present experiments showed that for UM_3 this works well for dilution but not so well for centerline geometry. The models assume the plume boundaries to be circular and centered about the centerline trajectory. In a dense jet, however, due to instabilities caused by the negative buoyancy, the top edge of the plume is closer to the center of mass than the bottom edge. This asymmetry in cross sectional profile is an unaddressed issue in all the models and seems to be the main reason for their poor predictions of flow geometry.

4.7.4 Discussion

Following early experiments of Zeitoun et al. 1972, the 60° jets were assumed to have the longest trajectory and maximum impact point dilution and were accepted as the standard design for dense discharges. In the present study, many experiments were done with varying nozzle angles using three dimensional laser-induced fluorescence (3DLIF) to map concentration fields. Discharges that inclined upwards at 15° to 85° were studied for conditions typical of oceanic outfalls. The 2D time-average concentration fields extracted from the center sheets of the 3D file were used to identify flow characteristics. Flow geometry and dilution at the location of maximum rise height, at impact point, and at the end of the near field were obtained. Normalized expressions were derived and plotted along with previously reported data. The rise heights were slightly higher than previous data and the locations of maximum height and impact point were in good agreement with reported data. The centerline dilution at terminal rise height and the location of the impact point were in general accordance with previous data. For the first time, the location of the near field and dilution at this point were measured for various nozzle angles. Near field dilutions were 10 to 35% higher than at the impact point, depending on nozzle angle. The largest increase in dilution, about 35%, occurred for nozzle angles of about 35° to 65°; for smaller and larger angles, the increase was about 10%. This caused the near field dilution to be somewhat more sensitive to nozzle angle although it varied little over the range of about 40° to 70° and 55° may afford slightly higher dilution than the generally accepted value of 60°.

Computational models were used to compare with the experimental results, except for the near field. (as integral models do not consider boundary interaction). Thus models are limited to the region up to the impact point. The models predicted the trends of experimental data, and thus were used to estimate the optimal angles of major parameters. They implied that the discharge reaches the highest centerline

dilution at the terminal rise height for 45°, and the maximum dilution at the impact point occurs for about 50°. The maximum near field dilution occurs for a nozzle angle of about 55°. The numerical models underestimate geometric properties in all cases, with CORJET and JETLAG being slightly closer. Dilutions were also underestimated, with UM_3 closest. The reason for the poor predictions of geometrical properties may be their assumption of radial symmetry, which was not observed in the experiments. Centerline dilution predictions may be in error because, in UM_3 and JETLAG, they are computed from concentration profiles that are assumed to be 3/2 power or Gaussian distribution respectively to find centerline values from averaged ones. The predictions of UM_3 for jet geometry were improved significantly by reducing the value of the aspiration coefficient from its default value of 0.1 to 0.05, whereas the default value gave good approximations for dilution. The results showed that entrainment models could be good alternatives for modeling dense jets in unlimited environments after validation, although it seems that the experiments are still the only way to predict jet further dilution beyond the impact point. The results imply that the optimum discharge angle for impact dilution is 50°, slightly less than the generally accepted value of 60°. If dilution at the near field is considered, 60° is still a good approximation. However, all of the dilution results were relatively insensitive to nozzle angle in the range 40°to 70°. Less steep angles can be used to limit rise height, for example, in shallow water conditions. This study underlines some issues in the use and application of commercial models that have not been previously considered. The results can help environmental authorities, promoters, and designers for better modeling of the near field in desalination brine discharge projects.

4.8 Dense Jet Discharges in Shallow Water

4.8.1 Introduction

The previous sections have considered dense discharges into deep waters that are unaffected by the water surface. As previously discussed, nozzle angles between 45° and 60° give the longest trajectory and highest dilution at the seafloor impact point and at the end of near field. However, higher angles increase the rise height and may cause impact with the surface in shallow coastal waters. If deep waters are not available, it is still necessary to design the discharge for efficient mixing with the surrounding ambient water. In shallow waters, the water available for jet entrainment and mixing and dilution may be decreased and the trajectory and flow geometry changed. Figure 90 shows a typical experiment for a 60° discharge impacting the surface in shallow waters.

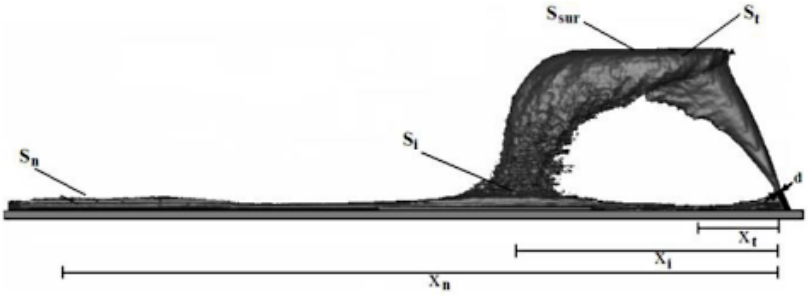

Figure 90. 60° inclined dense discharge in shallow water.

Ambient water bodies always have horizontal boundaries such as the water surface, seafloor, and pycnoclines. Depending on the dynamic and geometric characteristics of the discharge, a variety of interaction phenomena with these boundaries can occur. They can significantly influence the flow stability and change the mixing and dilution; this is known as the shallow condition. Shallow water diffuser studies are quite rare especially for brine discharges. Koester (1974) studied submerged thermal

discharges and suggested $h_{max}/H \leq 0.75$ where h_{max} is the jet maximum rise height and H the ambient depth as a criterion to delineate deep and shallow receiving water. His experiments showed that for $h_{max} \leq 0.75H$, the jet is typically unaffected by the bottom or surface boundary. The same criterion is used in CORMIX software to delineate deep and shallow water for brine discharges (Bleninger and Jirka 2008). So in CORMIX when the jet do not occupy more than 75% of the water depth, it is assumed to be the deep condition with no dynamic surface interactions.

Many large desalination plants are constructed or under construction in shallow coastal zones very close to shore. High capital cost, energy consumption, and environmental impacts have always been the main consideration in design and operation of desalination plants. There is a general desire to optimize the discharge efficiency while minimizing the high outfall construction cost by minimizing its length. But in shallow waters with varying tides, it is not always possible to achieve full submergence and surface contact may occur. Mixing when the flow contacts the water surface is not well understood ,and the objective of this study was to find out when and for which depth and dynamic conditions the flow is influenced by the water surface.

Three different orientations, 30°, 45°, and 60° were investigated for different Froude numbers and ambient depths and the flow characteristics for each angle were identified. A criterion is proposed for each nozzle angle to delineate deep from shallow water conditions.

4.8.2 Analysis

Figure 90 shows the main flow characteristics of a 60° inclined dense discharge in shallow, stagnant water. As discussed in previous sections the jet reaches a terminal rise height which in limited ambient depth and high Froude number is the water surface and then falls back to the floor. The flow then spreads as a density current. The terminal rise height of the jet, y_t could be equal to ambient depth, H, for shallow water at the horizontal distance x_t. The jet then leaves the water surface and impinges on the bottom at x_i where the dilution is S_i. Beyond the impact point additional mixing leads to an ultimate initial dilution Sn (the near field dilution) at the end of the near field whose length is x_n.

The analyses of this case follow that in Section 2 with the addition of a new parameter, the ambient depth H. With the usual assumptions, all the dependent variables of the flow field, φ, are functions of the discharge angle θ, and the jet kinematic fluxes of volume, Q, momentum, M, buoyancy, B, and ambient depth, H:

$$\varphi = f(Q, M, B, \theta, H) \qquad (15)$$

$$Q = \frac{\pi}{4} d^2 u; \quad M = uQ; \quad B = g'_o Q \qquad (16)$$

where $g'_o = g(\rho_o - \rho_a)/\rho_a$ is the modified acceleration due to gravity. Following dimensional analysis for geometrical distances (X) the non-dimensionalized expressions are:

$$\frac{\chi}{H} = f\left(\frac{d\mathsf{F}}{H}\right) \qquad (17)$$

and dilutions are non-dimensionalized as

$$\frac{Sd}{H} = f\left(\frac{d\mathsf{F}}{H}\right) \qquad (18)$$

In deep water, the ambient depth is not an important parameter. Although the empirical parameters for deep water have been mostly identified for different nozzle angles, no studies were found in the literature for shallow water.

4.8.3 Experiments

The experimental procedures were similar to the previous sections; the only change was that a horizontal sheet of Lucite was placed exactly on the water surface to avoid laser reflections at the surface and surface wave effects. The Froude number was varied from small to very large to simulate ambient water conditions ranging from deep to partially shallow and completely shallow.

The experiments and results are summarized in dimensionless form in Table A3. The parameters were chosen to include the typical range expected for desalination brine discharges. Three nozzle angles, 30°, 45°, and 60°, were studied; 94 experiments were done: 26 for 30°, 30 for 45° and 38 for 60° jets ranging from very deep to completely shallow condition. The nozzle diameter d was 0.317 cm and the nozzle tip was about 2 cm above the floor, i.e. h/d = 6.3. All the heights and ambient depth were measured from the floor, not the nozzle elevation.

Typical time-averaged three-dimensional flow visualizations for a 60° inclined jet in shallow water are shown in Figure 91. The outer surface is shown as a semi-transparent gray iso-concentration surface, whose level is approximately 10% of the maximum centerline concentration. Figure 91 also shows the two-dimensional concentration field (with concentration levels shown in false color) extracted from the centerline longitudinal plane. These central planes were used to extract the major flow properties as discussed below.

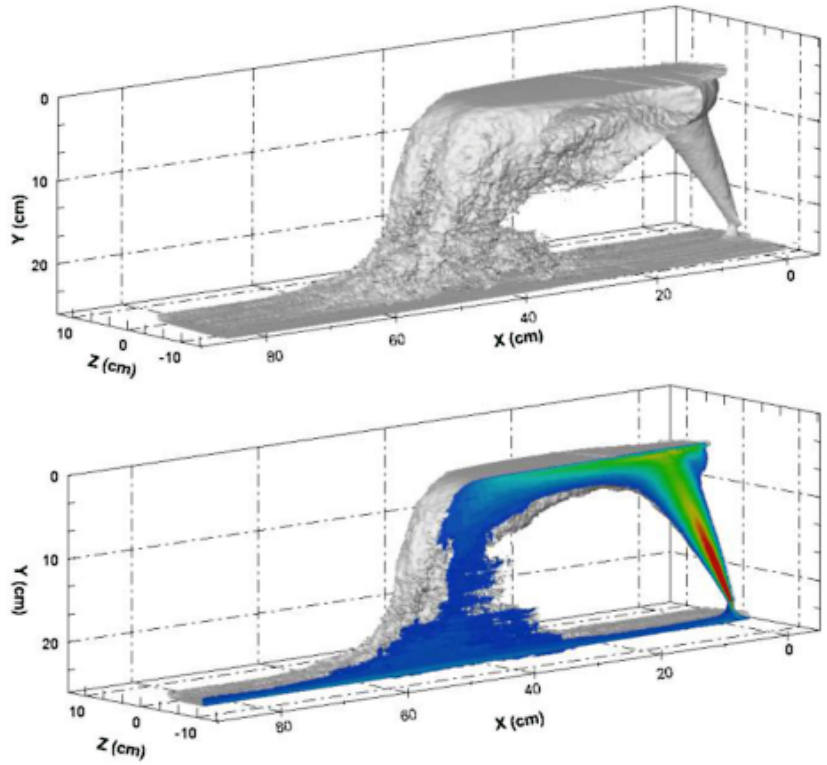

Figure 91. Three-dimensional time-averaged image and 2D planar sheet of flow for 60° dense jet in shallow water, dF/H = 1.03.

4.8.4 Results

Side views of 3D gray iso-concentration surfaces and central planar tracer fields for three nozzle angles in varying water depths are shown in Figure 92. The central planes are vertical and parallel to the jet direction and pass through the nozzle centerline (the x-y plane). The tracer concentration levels are shown in false-color contours. The images are typical of turbulent dense jets and show clearly the rising and falling behavior for flow in fully submerged conditions and surface attachment in shallow water for different angles. They show that jet trajectories are affected by the discharge angle and how increases in angle can change surface attachment. As the angle increases, the terminal rise height increases and the jet becomes more sensitive to water depth especially when it is relatively shallow. For the case of full submergence or deep condition, the flow has the regular behavior as reported previously and in many observations (Roberts et al. 1997, Kikkert et al 2006, Shao and Law, 2010, Abessi and Roberts, 2013). However, once the upper side of the jet reaches the water surface, entrainment and flow mixing change. The surface stops the jet's upward momentum but the horizontal momentum component combined with buoyancy-induced instability drives the flow downstream before sinking to the sea floor. In shallow water, due to the surface effect, the flow changes, mixing is inhibited and dilution decreases. These changes in flow and trajectory after surface impact are shown in Figure 92.

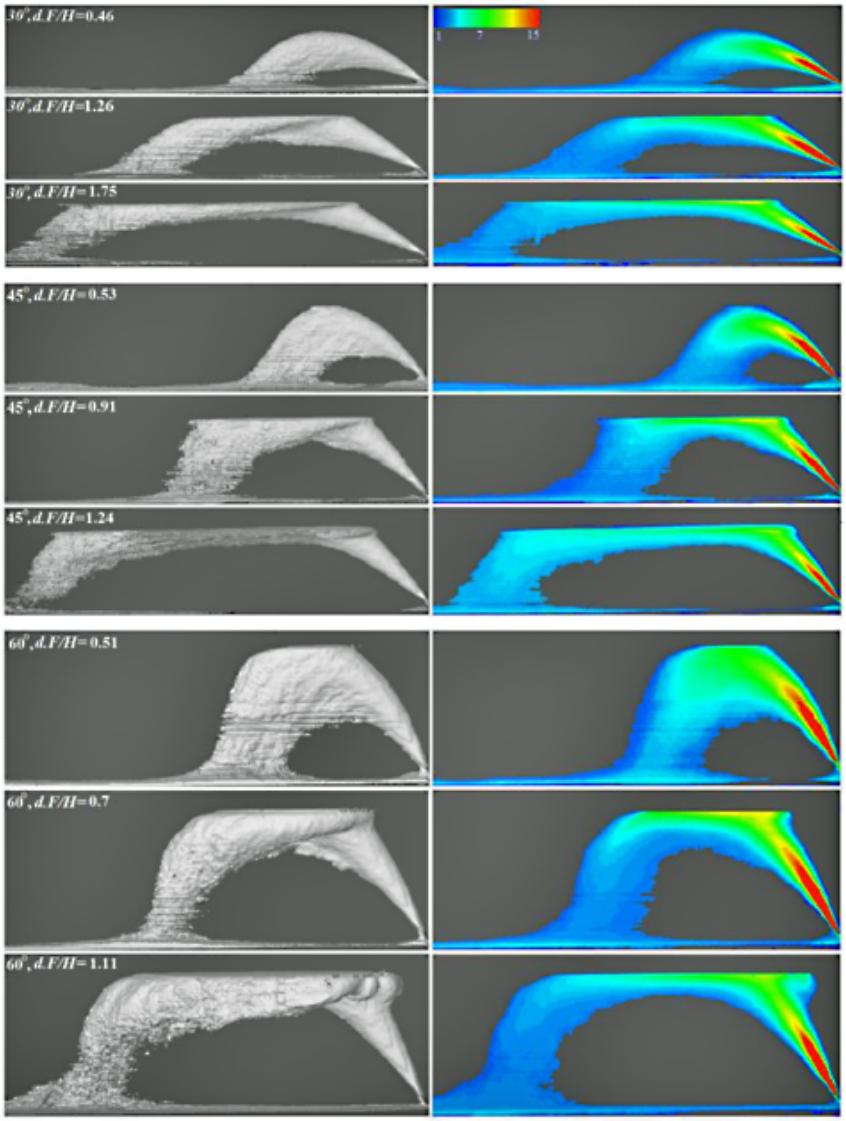

Figure 92. Flow configurations ranging from deep to shallow conditions for 30°, 45° and 60° jets.

Concentration profiles across the jets for three nozzle angles and various depths are shown in Figure 93. When the flow is fully submerged, the concentration profile can be compared with a typical Gaussian profile—although some deviation is observed in the inner half. This is attributed to the buoyancy-induced instability that has been reported in many previous studies (e.g. Bleninger and Jirka 2008, Kikkert et al., 2007, Shao and Law, 2010, Abessi and Roberts 2013). In limited water depth when the Froude number increases, the jet begins to partially impact the water surface. It limits the cross-sectional distribution of concentration and cuts off the Gaussian profile. The upper part of the flow impacts the water surface while the jet centerline is still beneath the surface. Slight increases in Froude number result in the jet completely touching the surface which cuts the flow centerline. Depending on the jet angle and Froude number, the flow can either immediately sink down or can attach to the surface for some distance downstream before detaching and descending. As shown in this figure, when the flow is in partial contact with the water surface, the concentration distribution is semi-Gaussian, but the concentration distribution completely deviates from Gaussian once the centerline reaches the water surface.

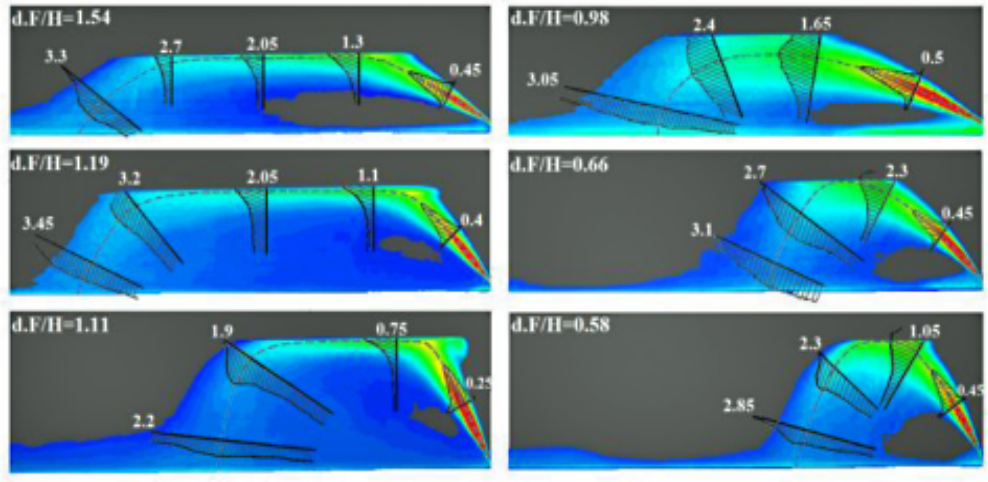

Figure 93. Changes in concentration profile along downstream in 30°, 45° and 60° dense jets.

As previously mentioned, the concentration distribution is fully Gaussian along the flow for discharge into deep water. It deviates from the standard Gaussian shape farther from the nozzle but remains bell-shaped. In partially shallow water (right images in Figure 93), the cross-sectional profile is initially Gaussian but impacting the water surface around maximum rise height, the surface cuts the upper part off and concentration distribution changes to semi Gaussian. In shallow water (left images in Figure 93), the concentration distribution changes from full to half Gaussian along the surface. For both, however, adjacent to the water surface when the negative buoyancy becomes dominant the flow sinks toward the floor and a Gaussian profile reforms in the descending phase. In these flows, the jet has limited depth so there is less opportunity to fully interact with ambient water near the surface and the jet can only spread and entrain from its lower sides. This inhibits entrainment near the water surface and decreases mixing and dilution. In very shallow condition and higher nozzle angles, the flow also experiences some re-entrainment which further limits dilution. It creates a type of unstable condition that is discussed in more detail in the following paragraph.

The major geometrical and mixing parameters (defined in Figure 90) for different angles were extracted from the 2D time average concentration fields using the methods discussed previously. The nozzle was elevated above the floor ($h/d \approx 6.3$), and rise heights were measured from the ambient floor. The horizontal locations of the impact point and the near field were measured from the nozzle tip. The results are plotted in the dimensionless form of Eqs. 17 and 18 as functions of $d\mathsf{F}/H$ for different nozzle angles in Figures 94 to 100.

In deep water, the flow does not have sufficient momentum to reach the water surface and the tracer concentration is essentially zero on the surface, (i.e., the surface dilution is infinite). But once the flow reaches the water surface, tracer concentrations dramatically increase from minimum for jet terminal rise height to maximum for jet centerline. Once the upper part of the jet impacts the water surface, the deep condition transitions to shallow condition. But when the jet centerline intersects the surface, the water is considered to be completely shallow. The surface dilution decreases from infinity for deep conditions to an asymptotic constant value for large Froude numbers when the centerline reaches the water surface. In the transition from deep to completely shallow, the flow passes through a partly shallow regime. This represents the condition that the jet is already in contact with the surface on the upper side, but the centerline is still below the surface. Therefore, inclined dense discharges pass from deep to completely shallow water through a transition (partially shallow) condition. In the completely shallow condition, instabilities and re-entrainment occur.

The surface dilution for 30° jets is shown in Figure 94. It decreases rapidly from infinity to $S_{sur}/F < 0.05$ between $dF/H = 0.87$ to 1.5; this is the partly shallow condition for 30° dense jets. The corresponding ranges are about dF/H = 0.54 to 0.85 and $dF/H = 0.47$ to 0.80 for 45° and 60° jets, respectively. Due to the flow configurations for different jet angles, the range of occurrence for partially shallow water is smaller for 45° and 60° jets, about 0.32, than for 30° jets, about 0.63. This means that partly shallow condition is more probable and extends longer for smaller angles. The relatively large values of dF/H for the 30° jet shows the lessened probability of surface contact for smaller angles. In the following figures, the transition from deep to shallow flow is better shown for the horizontal location of centerline maximum height.

The horizontal location (x_t) of the centerline maximum height for partly shallow water is just below the water surface and for completely shallow water is at the surface. x_t is plotted in Figure 95 for different nozzle angles. For all angles, x_t/dF is initially constant for deep water condition, then decreases as it approaches the completely shallow condition. As mentioned before, the transition is steeper for 45° and 60° jets than for 30°. For 30° jets, x_t/dF is initially about 1.95 and reduces to less than 0.9 for the completely shallow condition. The corresponding values of x_t/dF for 45° and 60° jets in deep conditions are about 2.05 and 1.85, and for shallow condition are less than 1.0 and 0.7, respectively.

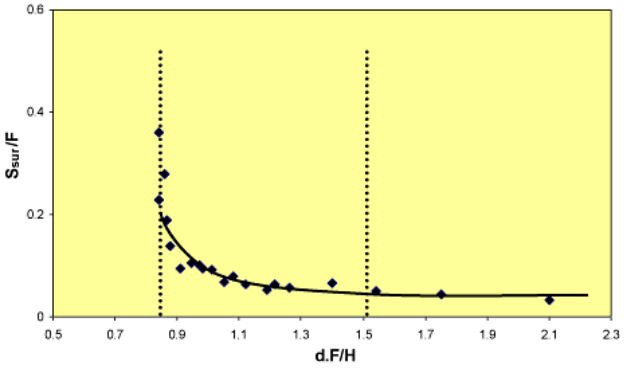

Figure 94. Surface dilution for 30° jet in various ambient depth conditions.

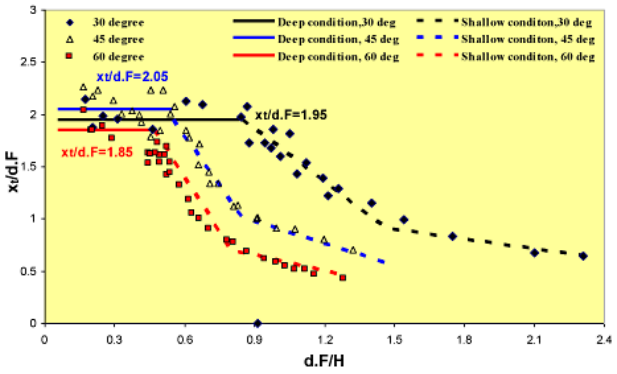

Figure 95. The horizontal location of centerline maximum height for 30°, 45° and 60° jets in deep and shallow waters.

Dilutions at the maximum centerline height S_t for different jet angles in deep and shallow conditions are plotted in Figure 96. When the jet is fully submerged, S_t/F is a constant equal to 0.52 for 30° and 0.6 for 45° and 60° jets, but as the Froude number increases the jet contacts the water surface. The jet then passes through a transition where S_t/F decreases rapidly before reaching a constant asymptotic value ($S_t/F < 0.1$) for large dF/H in completely shallow conditions. The figure shows how surface contact influences jet mixing and centerline dilution when reaching the water surface while the centerline is still below the water surface. For higher dF/H when the surface intersects the jet centerline, dilution is no longer changing and becomes constant. The ranges of dF/H observed for transition are in general agreement with those mentioned above for different nozzle angles.

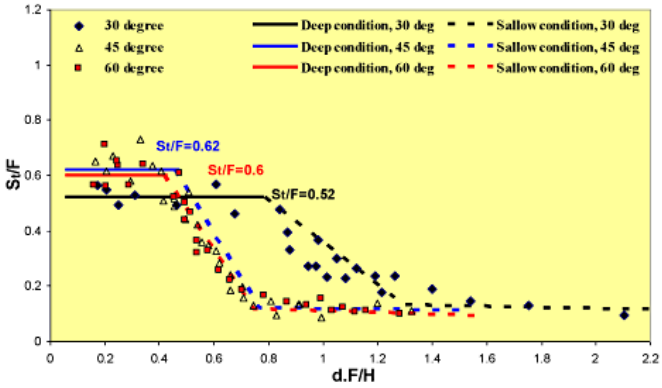

Figure 96. Dilution at centerline maximum height for 30°, 45° and 60° dense jets in deep and shallow waters.

In Figure 97, the location of the jet impact point for deep and shallow conditions is plotted in dimensionless form for 30°, 45°, and 60° jets. The location is defined as the horizontal distance of the jet from nozzle tip to impact point. The solid lines show the variation of x_i/dF versus dF/H for deep water and dotted lines for shallow water. As shown in this figure, despite the notable changes in the flow, surface contact over a wide range of dF/H only slightly changes the impact point location. The vertical component of jet momentum is destroyed on surface impingement. Part of it converts to horizontal momentum and is the reason for slight increases in the slope of dotted lines in shallow water. However, this is only true up to specific dF/H. As exhibited in Figure 93, for very large Froude numbers, re-entrainment in the limited depth of ambient water, pushes the flow to an unstable condition which limits the jet horizontal displacement. As shown in Figure 97 for small dF/H, the impact point location, x_i/dF is constant at 3.47 for 30° jets and 3.5 and 2.7 for 45° and 60°. It passes a transition zone then decreases to much lower values as the flow becomes completely shallow. Increases in Froude numbers do not significantly change the impact point location in the transition region.

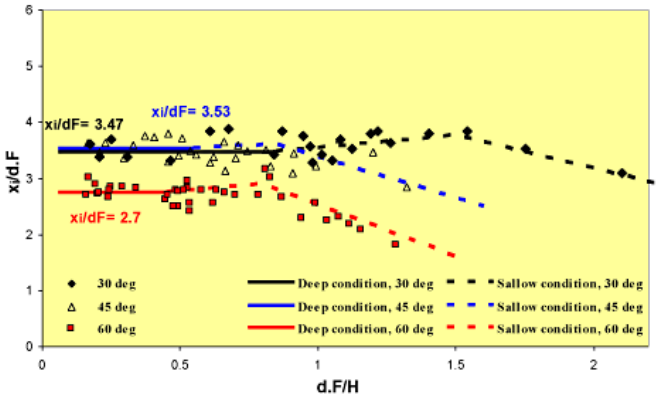

Figure 97. Impact point location for 30°, 45° and 60° jets in deep and shallow condition.

Figure 98 shows the minimum dilution at the impact point (S_i), S_i/F is initially constant for the full submergence condition. Then, as F increases, the mixing regime changes to the shallow condition and S_i/F decreases. The changes in impact point dilution occur even before the upper part of the jet impinges on the water surface. For deep water conditions, $S_i/F = 1.1$ for 30° jets and 1.6 for 45° and 60°, then the S_i/F decreases to less than 0.55 for 30° jets and 0.85 for 45° and 60° dense jets for completely shallow water. Interestingly, in limited ambient depth (large dF/H), for transition shallow 30° jets result in higher impact point dilution than 45° and 60°. In many previous studies (Zeitoun et al. 1971 and Shao and Law 2010) it is reported that for 30°, the impact point dilution is less than higher angles because of the shorter flow trajectory for smaller angles. But in transition shallow conditions, the longer flow trajectory under the water surface gives more opportunity for mixing and dilution for the 30° jet than 45° and 60°. Therefore, in receiving water with limited depth, 30° may be a good option for brine discharge because it is less engaged with the surface and has more opportunity to entrain ambient water and dilute before impacting the floor.

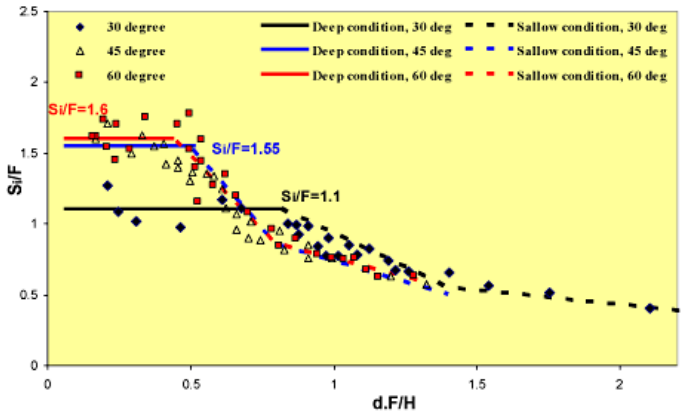

Figure 98. Impact point dilution for 30°, 45° and 60° jets in deep and shallow conditions.

Beyond the impact point, the flow spreads as a density current and continues to entrain and mix with ambient water. This additional dilution beyond the impact point was reported by Roberts et al. (1997). The location where the turbulence and vortices collapse is suggested to define the end of the near field, which is usually considered to be the location where water quality standards must be met. Figure 99 shows the near field location for various discharge angles, for deep and shallow condition. In the present study, like before, the near field is defined as the location where little further dilution occurs downstream, i.e. where the change of dilution is less than 5%. As shown in Figure 99 for deep water, the near field length, x_n/dF, is initially constant, but after surface impingement x_n/dF substantially decreases. The present results show that in shallow water conditions, the water surface limits the jet maximum rise height to the water depth and subsequently diminishes jet entrainment and mixing during the descending phase. So, unlike the impact point, the length of the near field x_n/dF for the shallow conditions decreases substantially compared to deep water. The value of x_n/dF was only obtained for smaller dF/H due to experimental limitations.

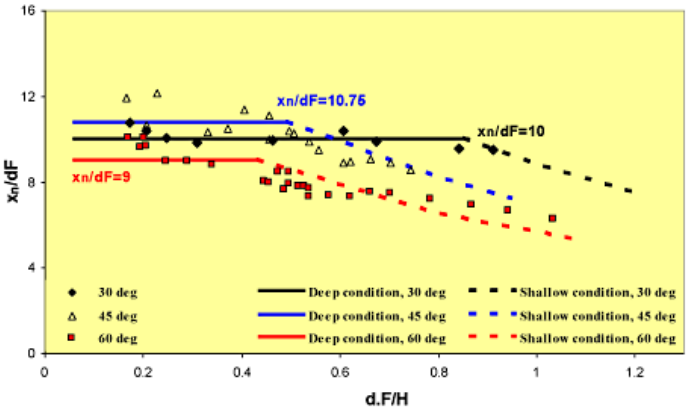

Figure 99. Near field location for 30°, 45° and 60° jets in deep and shallow conditions.

Dilution at the near field was obtained for the various angles and is plotted in Figure 100 for deep and shallow conditions. This figure shows how surface impingement restricts mixing and dilution. For deep water, the near field dilution, S_n/F, is initially constant equal to 1.85 for 30° jet and 2.5 and 2.6 for 45° and 60° jets respectively. But once the jet impacts the water surface, S_n/F decreases substantially. Decreases for 30° compared to 45° and 60° clearly show the importance of ambient depth, even in shallow conditions, as 45° and 60° jets have longer descending paths than 30°. This induces more energy during jet descent with more opportunity for flow dilution along the floor.

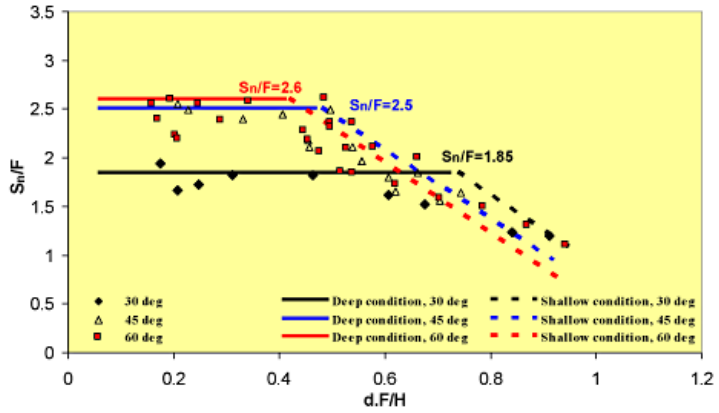

Figure 100. Near field dilution for 30°, 45° and 60° dense jets in deep and shallow conditions.

4.8.5 Discussion

Comprehensive laboratory experiments were conducted on dense discharge in shallow water for various angles. The results show that shallow water can affect jet dynamics and mixing.

REFERENCES

Abessi, O., M. Saeedi, T. Bleninger, and M. Davidson. (2012) “Surface discharge of negatively buoyant effluent in unstratified stagnant water.” Journal of Hydro-environment Research, 1-13.

Cederwall, K. (1968). “Hydraulics of Marine Wastewater Disposal.” Hydraulics Division, Chalmers Institute of Technology, Sweden. Report No.42.

Cipollina, A., A. Brucato, F. Grisafi, and S. Nicosia (2005). “Bench-scale investigation of inclined dense jets.” Journal of Hydraulic Engineering, ASCE 131(11), 1017-1022.

Fischer, B., J.E. List, J. Imberger, and H.N. Brooks (1979). ‘Mixing in Inland and Coastal Waters.’ Academic Press, INC. San Diego, California.

Gungor, E. and P.J.W. Roberts (2009). "Experimental Studies on Vertical Dense Jets in a Flowing Current." Journal of Hydraulic Engineering, 135(11), 935-948.

Jiang, B, A.W.K. Law and J.H.W Lee (2012a). “Mixing of 45 Inclined Dense Jets in Shallow Coastal Waters: Surface Impact Dilution.” Journal of Hydraulic Engineering, ASCE.

Kikkert, G.A., M.J. Davidson, and R.I. Nokes (2007). “Inclined negatively buoyant discharges.” Journal of Hydraulic Engineering, ASCE 133(5), 545-554.

Lai C.K.C. and J.H.W. Lee (2012). “Mixing of inclined dense jets in stationary ambient.” Journal of Hydro-Environment Research, 6, 9-28.

Nemlioglu, S. and P.J.W. Roberts (2006). “Experiments on dense jets using three-dimensional laser-induced fluorescence (3DLIF).” Proceedings of the 4th International Conference on Marine Waste Water Disposal and Marine Environment.

Palomar P., J.L. Lara, I.J. Losada, M. Rodrigo, and A. Alvárez (2012a). “Near field brine discharge modeling part1: Analysis of commercial tools.” Desalination 290, 14–27.

Palomar P., J.L. Lara, I.J. Losada, M. Rodrigo, and A. Alvárez (2012b). “Near field brine discharge modeling part 2: Validation of commercial tools.” Desalination 290, 28–42.

Papakostantis, I.G., G.C. Christodoulou, and P.N. Papanicolaou (2011a). “Inclined Negatively buoyant jets 1: geometrical characteristics.” Journal of Hydraulic Research 49(1), 3-12.

Papakostantis, I.G., G.C. Christodoulou, and P.N. Papanicolaou (2011b). “Inclined negatively buoyant jets2: concentration measurements.” Journal of Hydraulic Research 49(1), 13-22.

Roberts, P.J.W., Ferrier, A., and Daviero, G. J. (1997). "Mixing in Inclined Dense Jets." Journal of Hydraulic Engineering, ASCE, 123(8), 693-699.

Shao, D., and A.W.-K. Law (2010). “Mixing and boundary interactions of 30◦ and 45◦ inclined dense jets.” Environmental Fluid Mechanics. 10, 521–553

Shao, D., and A.W.-K. Law (2011). “Boundary impingement and attachment of horizontal offset dense jets.” Journal of Hydro-Environment Research, 5(1), 15-24.

Tian, X. (2002). "3DLIF and Its Applications to Studies of the Near Field Mixing of Wastewater Discharges." PhD Thesis, School of Civil and Environmental Engineering, Georgia Institute of Technology, Atlanta, Ga.

Tian, X., and P.J.W. Roberts, (2003). "A 3D LIF System for Turbulent Buoyant Jet Flows." Experiments in Fluids, 35, 636-647.

Tian, X., P.J.W. Roberts, and G.J. Daviero, G.J. (2004). "Marine Wastewater Discharges From Multiport Diffusers I: Unstratified Stationary Water." Journal of Hydraulic Engineering, 130(12), 1137-1146. Wright, S.J. (1984). Buoyant jets in density-stratified crossflow. Journal of Hydraulic Engineering 110(5), 643-656.

Zeitoun, M.A., R.O. Reid, W.F. McHilhenny, and T.M. Mitchell (1970). “Model Studies of Outfall System for Desalination Plants.” Research and Development Progress Rep.804. Office of Saline Water, U.S. Department of Interior, Washington, D.C.

Zeitoun, M.A., R.O. Reid, W.F. McHilhenny, and T.M. Mitchell (1972). “Model studies of outfall systems for desalination plants. Part III. Numerical simulation and design consideration.” Res. and Devel. Progress Rep, No 804, Office of Saline Water, U.S. Department of the Interior, Washington, D.C.

APPENDIX – SUMMARY OF EXPERIMENTS

The experimental data are summarized in these appendices.

Table A1. Stationary Multiport Experiments (Section 4.1)

F	$s/(dF)$	$y_t/(dF)$	$x_i/(dF)$	S_i/F	$x_n/(dF)$	S_n/F	ID	No. of ports	No. of sides
15.66	1.74	2.19	2.97	1.59	9.02	1.99	31 Jan-Exp01	22	Two
25.45	1.07	1.83	2.16	1.07	6.05	1.19	31 Jan-Exp02	22	Two
15.66	1.74	2.39					31 Jan-Exp03	22	Two
11.98	2.27	2.39	2.63	1.98		2.45	1 Feb-Exp01	22	Two
23.97	1.13	1.90	2.57	1.12		1.30	1 Feb-Exp02	22	Two
35.96	0.76	1.53					1 Feb-Exp03	22	Two
16.95	1.61	2.38	2.91	1.28	8.67		2 Feb-Exp02	22	Two
33.91	0.81	1.66	1.79	0.51			2 Feb-Exp03	22	Two
44.08	0.62	1.53	1.70				2 Feb-Exp04	22	Two
15.66	1.74	1.97		1.33			6 Feb-Exp01	22	Two
19.57	1.39	1.90	2.26				6 Feb-Exp02	22	Two
33.91	0.81	1.66	1.48	0.46			8 Feb-Exp01	22	Two
44.08	0.62	1.51	1.30	0.36			8 Feb-Exp02	22	Two
49.17	0.55	1.58	1.34	0.37			8 Feb-Exp03	22	Two
61.04	0.44	1.37	1.38	0.28			8 Feb-Exp04	22	Two
35.96	0.76	1.66	1.64	0.57	5.18	0.69	10 Feb-Exp01	22	Two
47.95	0.57	1.62	1.34	0.34		0.52	10 Feb-Exp02	22	Two
27.12	1.00	1.95	2.24	0.76		0.85	14 Feb-Exp01	22	Two
33.91	0.81	1.63		0.59	4.75	0.70	14 Feb-Exp03	22	Two
17.34	1.70	2.64	2.74	1.80	11.00	2.26	16 Feb-Exp01	7	One
34.70	0.85	1.75	2.01	0.75	6.70	0.96	16 Feb-Exp02	7	One
52.03	0.57	1.60	1.73	0.50		0.68	16 Feb-Exp03	7	One
63.07	0.47	1.67	1.72	0.39	4.76	0.56	16 Feb-Exp04	7	One
56.76	0.52	1.63	1.77	0.51	4.92	0.58	16 Feb-Exp05	7	One
63.07	0.47		1.72	0.41	4.84	0.58	16 Feb-Exp06	7	One
110.38	0.53	1.23	1.66	0.46			16 Feb-Exp07	4	One
62.91	0.94	1.86	1.89	0.83	6.17	0.93	16 Feb-Exp08	4	One
56.84	1.04	1.89	1.82	0.66	5.37	1.17	21 Feb-Exp01	4	One
34.77	1.70	1.94					21 Feb-Exp03	4	One
77.27	0.76	1.63	1.93	0.83	4.29	0.80	21 Feb-Exp04	4	One
99.34	0.59	1.40	1.82	0.79			21 Feb-Exp05	4	One
81.11	0.73	1.54	1.93	0.79	3.96	0.91	21 Feb-Exp06	4	One
63.09	0.93	1.76	1.80	0.99			21 Feb-Exp07	4	One
27.03	2.19	2.10	2.39		8.62		21 Feb-Exp09	4	One
18.02	3.28	2.37	2.80			3.08	21 Feb-Exp10	4	One
24.49	4.39	2.14	2.47	1.70			23 Feb-Exp01	1	One
39.18	7.14	2.00	2.78	1.82			23 Feb-Exp02	1	One
48.98	5.71		2.75	1.85			23 Feb-Exp03	1	One
24.49	11.43	2.17	2.66	2.04		2.55	23 Feb-Exp04	1	One
19.59	3.14	2.27	3.06	1.62	10.30	2.55	23 Feb-Exp05	1	One
29.39	9.52	2.00	3.08	1.21			23 Feb-Exp06	1	One
34.29	8.16	2.00	2.87				23 Feb-Exp07	1	One

Table A1. Stationary Multiport Experiments (Section 4.1)

F	$s/(dF)$	$y_i/(dF)$	$x_i/(dF)$	S_i/F	$x_n/(dF)$	S_n/F	ID	No. of ports	No. of sides
44.08	6.35		2.57			2.16	23 Feb-Exp08	1	One
59.99	4.66		2.77	1.45		3.33	28 Feb-Exp01	1	One
47.99	5.83		2.98	1.54			28 Feb-Exp02	1	One
35.99	7.77	1.98	3.03	1.54			28 Feb-Exp03	1	One
23.99	11.66	2.33	2.88	1.73	11.53	3.20	28 Feb-Exp04	1	One
29.99	9.33	2.11	2.94	1.48	8.41	3.17	28 Feb-Exp05	1	One
41.99	5.12	1.94	2.82	1.75	7.25	3.17	28 Feb-Exp06	1	One
53.99	3.98		2.22	1.40	7.97		28 Feb-Exp07	1	One

Table A2. Inclined Nozzle Stationary Experiments (Section 4.7)

Nozzle Angle	F	L_M	y_m/L_M	y_t/L_M	x_t/L_M	S_t/F	Xi $/L_M$	S_i/F	x_n/L_M	S_n/F	ID
15	52.16	15.57	0.46	0.82	1.61	0.39	2.70	0.67			3 Oct-Exp1
15	26.08	7.78	0.57	0.89	1.80	0.40	3.08	0.96			3 Oct-Exp2
15	36.51	10.90	0.52	0.86	1.93	0.40	3.03	1.00	9.73	0.91	3 Oct-Exp3
15	46.94	14.01	0.46	0.80	1.78	0.36		0.85			3 Oct-Exp4
15	20.86	6.23	0.55	0.97	1.93	0.36	3.21	1.00	9.80	1.06	3 Oct-Exp5
15	31.29	9.34	0.51	0.85	1.71	0.34	2.94	0.95	10.06	1.33	3 Oct-Exp6
20	26.08	7.78	0.53	0.91	1.79	0.33	3.47	1.03	10.92	1.04	24Oct-Exp9
20	31.29	9.34	0.50	0.85	1.84	0.36	3.11	0.73	9.96	0.97	24Oct-Exp10
30	26.08	7.78	1.01	1.39	2.00	0.55	3.60	1.30	11.05	1.67	4 Oct-Exp1
30	39.12	11.67	0.92	1.33	2.08	0.53	3.60	1.02	10.45	1.83	4 Oct-Exp2
30	31.29	9.34	1.02	1.39	2.11	0.49	3.92	1.08	10.71	1.73	4 Oct-Exp3
30	21.91	6.54	1.13	1.53	2.28	0.56	3.84	1.43	12.24	1.94	4 Oct-Exp4
40	31.29	9.34	1.11	1.54	2.14	0.63	3.55	1.45	10.17	2.06	17Oct-Exp1
40	26.08	7.78	1.34	1.79	2.39	0.61	3.79	1.37	10.92	1.87	17Oct-Exp2
40	26.08	7.78	1.31	1.74	2.36	0.55	3.75	1.24	11.82	1.74	17Oct-Exp3
45	26.08	7.78	1.80	2.26	2.31	0.62	3.73	1.74	11.05	2.56	4 Oct-Exp5
45	41.73	12.45	1.55	2.02	2.27	0.58	3.57	1.50			4 Oct-Exp6
45	28.69	8.56	1.66	2.18	2.37	0.70	3.91	1.74	13.55	2.49	4 Oct-Exp7
45	20.86	6.23	1.93	2.41	2.41	0.65	3.85	1.60	13.41	1.84	4 Oct-Exp8.
50	26.08	7.78	1.84	2.24	2.12	0.79	3.47	1.83	10.79	2.56	9 Oct-Exp1
50	41.73	12.45	1.55	2.02	1.93	0.68	3.21	1.71	8.99	1.92	9 Oct-Exp2
50	20.86	9.34	1.75	2.31	2.20	0.85	3.44	1.81	10.71	2.28	9 Oct-Exp3
50	31.29	6.23	1.86	2.40	2.21	0.74	3.53	1.72	12.85	2.04	9 Oct-Exp4
55	20.08	7.78	1.97	2.56	2.13	0.67	3.42	1.50	11.31	2.04	9 Oct-Exp5
55	41.73	12.45	1.76	2.28	2.09	0.75	3.27	1.71	9.24	1.92	9 Oct-Exp6
55	31.29	9.34	1.99	2.44	1.95	0.82	3.27	1.77	10.49	2.07	9 Oct-Exp7
55	20.86	6.23	2.25	2.73	2.28	0.94	3.63	1.92	12.85	2.34	9 Oct-Exp8
60	31.29	9.34	1.90	2.57	2.00	0.69	3.08	1.88	9.53	2.00	11Oct-Exp1
60	21.38	6.38	2.14	2.66	2.16	0.74	3.29	1.61	11.75	2.40	11Oct-Exp2
60	25.56	7.63	1.95	2.44	1.97	0.73	2.88	1.86	10.69	2.17	11Oct-Exp3
60	36.51	10.90	1.82	2.33	1.88	0.53	3.03	1.52	9.50	2.38	11Oct-Exp4
60	26.08	7.78	2.24	2.69	1.96	0.54	3.21	1.45	10.28	2.19	17Oct-Exp4
65	28.69	8.56	2.07	2.67	1.52	0.54	2.55	1.48			11Oct-Exp5
65	36.51	10.90	2.10	2.52	1.59	0.48	2.65	1.56	8.63	1.69	11Oct-Exp6
65	31.29	9.34	2.17	2.61	1.66	0.47	2.75	1.40	8.89	1.73	11Oct-Exp7
65	26.08	7.78	2.26	2.81	1.71	0.50	2.76	1.50	9.44	1.92	11Oct-Exp8
65	20.86	6.23	2.46	3.02	1.90	0.56	2.64	1.65	11.24	2.08	11Oct-Exp9
70	26.08	7.78	2.51	3.06	1.48		2.38	1.83	9.96	2.32	23Oct-Exp1
70	31.29	9.34	2.39	2.89	1.51	0.50	2.44	1.77	8.62	1.60	23Oct-Exp2
70	26.08	7.78	2.40	2.98	1.50	0.57	2.39	1.47	11.13	1.87	23Oct-Exp3
70	20.86	6.23	2.55	3.18	1.61	0.52	2.36	1.60	12.21	2.08	23Oct-Exp4
75	25.56	7.63	2.30	2.91	1.16	0.57	1.67	1.86	8.29	2.06	24Oct-Exp1

Table A2. Inclined Nozzle Stationary Experiments (Section 4.7)

Nozzle Angle	F	L_M	y_m/L_M	y_t/L_M	x_t/L_M	S_t/F	X_i/L_M	S_i/F	x_n/L_M	S_n/F	ID
75	31.29	9.34	2.42	2.87	1.19	0.48	1.91	1.52	8.41	1.83	24Oct-Exp2
75	20.86	6.23	2.55	3.12	1.12	0.50	1.90	1.77	8.27	1.92	24Oct-Exp3
80	26.08	7.78	2.55	3.01	1.04	0.36	1.63	1.24	8.99	1.42	24Oct-Exp4
80	31.29	9.34	2.44	2.96	1.00	0.32	1.84	1.12	8.35	1.42	24Oct-Exp5
80	26.08	7.78	2.57	3.19	1.12	0.43	1.82	1.53	9.77	1.67	24Oct-Exp6
85	26.08	7.78	2.24	2.84	0.54	0.35	0.87	1.13	7.71	1.42	24Oct-Exp7
85	26.08	7.78	2.24	2.84	0.54	0.35	0.87	1.13	7.71	1.42	24Oct-Exp8

Table A3. Summary of Shallow Water Experiments (Section 4.8)

Angle	F_r	dF/H	$S_{sur}d/H$	S_td/H	x_t/H	x_i/H	S_id/H	x_n/H	S_nd/H	Exp ID
30	28.75	0.61		0.34	1.29	2.33	0.74	6.57	0.98	14 Jan Exp1
30	31.94	0.68		0.31	1.48	2.68	0.75	7.87	1.03	14 Jan Exp2
30	38.33	0.87	0.37	0.34	1.80	3.39	0.86	9.71		14 Jan Exp3
30	42.51	0.88	0.27	0.29	1.51	3.54	0.81			14 Jan Exp4
30	44.72	0.95	0.22	0.26	1.63	3.54	0.80			14 Jan Exp5
30	46	0.97	0.22	0.26	1.63	3.47	0.75			14 Jan Exp6
30	47.91	1.01	0.21	0.23	1.62	3.47	0.78			14 Jan Exp8
30	51.11	1.08	0.19	0.25	1.55	4.00	0.85			14 Jan Exp9
30	57.5	1.22	0.17	0.22	1.48	4.67	0.82			14 Jan Exp10
30	26.08	0.21		0.11	0.39	0.70	0.27	2.15	0.34	4 Oct Exp1
30	39.29	0.31		0.16	0.61	1.05	0.32	3.05	0.57	4 Oct Exp2
30	31.29	0.25		0.12	0.49	0.92	0.27	2.50	0.43	4 Oct Exp3
30	21.9	0.17		0.10	0.37	0.63	0.25	2.00	0.34	4 Oct Exp4
30	36.51	0.46		0.20	0.81	1.49	0.45	4.60	0.60	13 Feb Exp1
30	31.29	0.84	0.80	0.40	1.66	2.88	0.84	8.05	0.99	13 Feb Exp2
30	33.9	0.91	0.35				0.90	8.64	1.10	13 Feb Exp3
30	36.51	0.98	0.38	0.36	1.83	2.97	0.88			13 Feb Exp4
30	39.12	1.05	0.30	0.32	1.91	3.48	0.90	9.10		13 Feb Exp5
30	41.73	1.12	0.29	0.30	1.73	3.95	0.93			13 Feb Exp6
30	44.34	1.19	0.26	0.28	1.66	4.53	0.88			13 Feb Exp7
30	46.96	1.26	0.25	0.30	1.63	4.58	0.84			13 Feb Exp8
30	52.16	1.40	0.27	0.38	1.62	5.32	0.92			13 Feb Exp9
30	57.38	1.54	0.24	0.32	1.53	5.91	0.87			13 Feb Exp10
30	65.2	1.75	0.24	0.33	1.46	6.18	0.90			13 Feb Exp11
30	78.25	2.10	0.21	0.28	1.43	6.52	0.85			13 Feb Exp12
30	86.07	2.31	0.26	0.32	1.50	6.39	0.91			13 Feb Exp13
45	25.55	0.41		0.25	0.81	1.52	0.63	4.60	0.99	16 Jan Exp1
45	28.75	0.46		0.23	1.02	1.73	0.66	5.05	0.96	16 Jan Exp2
45	31.94	0.51	0.28	0.27	1.13	1.89	0.69	5.20	0.93	16 Jan Exp3
45	35.13	0.56	0.20	0.20	1.16	1.91	0.75	5.30	1.00	16 Jan Exp4
45	38.33	0.61	0.20	0.20	1.12	1.99	0.75	5.43	1.09	16 Jan Exp5
45	41.52	0.66	0.12	0.12	1.00	2.40	0.70			16 Jan Exp6
45	44.72	0.71	0.11	0.11	0.95	2.55	0.72			16 Jan Exp7
45	51.11	0.81	0.12	0.12	0.91	2.84	0.77			16 Jan Exp8
45	57.5	0.91	0.12	0.12	0.93	3.15	0.77			16 Jan Exp9
45	20.86	0.33		0.26	0.67	1.19	0.54	3.42	0.79	22 Jan Exp1
45	23.47	0.37		0.24	0.76	1.40	0.58	3.92		22 Jan Exp2
45	26.08	0.41		0.21	0.80		0.59			22 Jan Exp3
45	28.69	0.45		0.22	0.81	1.50	0.63	4.55	0.99	22 Jan Exp4
45	31.29	0.50	0.79	0.22	0.92	1.69	0.65	5.15	1.24	22 Jan Exp5
45	33.9	0.54	0.23	0.23	1.08	1.88		5.33	1.13	31 Jan Exp1
45	36.51	0.58	0.20	0.20			0.77			31 Jan Exp2

Table A3. Summary of Shallow Water Experiments (Section 4.8)

Angle	F_r	dF/H	$S_{sur}d/H$	S_td/H	x_t/H	x_i/H	S_id/H	x_n/H	S_nd/H	Exp ID
45	39.12	0.62	0.18	0.18	1.10	2.10	0.69	5.55	1.02	31 Jan Exp3
45	41.73	0.66	0.16	0.16	1.14	2.08	0.63	6.00	1.22	31 Jan Exp4
45	44.34	0.70	0.14	0.14	1.02	2.37	0.63	6.25	1.09	31 Jan Exp5
45	46.94	0.74	0.10	0.10	1.00	2.59	0.66	6.40	1.22	31 Jan Exp6
45	52.19	0.83	0.08	0.08	0.94	2.65	0.67			31 Jan Exp7
45	57.38	0.91	0.12	0.12	0.92	2.82	0.69			31 Jan Exp8
45	62.59	0.99	0.09	0.09	0.91	3.19	0.75			31 Jan Exp9
45	67.81	1.07			0.92	4.18				31 Jan Exp10
45	75.64	1.20	0.16	0.17	0.91	4.33	0.79			31 Jan Exp11
45	83.46	1.32	0.15	0.14	0.88	3.75	0.75			31 Jan Exp12
45	26.08	0.21		0.16	0.45	0.73	0.36	2.15	0.53	4 Oct Exp5
45	41.73	0.29		0.18	0.63	0.99	0.44			4 Oct Exp6
45	28.69	0.23		0.16	0.51	0.84	0.40	2.90	0.57	4 Oct Exp7
45	20.86	0.17		0.11	0.38	0.60	0.26	2.13	0.36	4 Oct Exp8
60	35.13	0.45			0.68	1.16	0.56	3.59	1.01	8 Jan Exp1
60	38.33	0.49			0.84	1.35		3.71	1.27	8 Jan Exp2
60	41.52	0.53			0.89	1.61		4.12	1.10	8 Jan Exp3
60	49.83	0.63			0.67	1.87				8 Jan Exp5
60	63.89	0.81			0.62	2.53	0.65			8 Jan Exp6
60	35.13	0.45			0.72					8 Jan Exp7
60	41.52	0.53			0.75	1.55				8 Jan Exp8
60	31.29	0.25		0.17	0.47	0.72	0.47	2.23	0.50	11 Oct Exp1
60	21.38	0.17		0.13	0.35	0.53	0.27	1.85	0.41	11 Oct Exp2
60	25.56	0.20		0.15	0.38	0.55	0.38	2.04	0.44	11 Oct Exp3
60	36.51	0.29		0.15	0.51	0.83	0.44	2.59	0.69	11 Oct Exp4
60	26.08	0.21		0.11	0.38	0.63	0.30	2.00	0.45	17 Oct Exp4
60	23.99	0.19				0.56	0.34	1.88	0.51	28 Feb Exp4
60	29.99	0.24				0.72	0.36			28 Feb Exp4
60	41.99	0.34				0.96	0.60	3.00	0.81	28 Feb Exp6
60	19.59	0.16				0.43	0.26		0.41	23 Feb Exp5
60	29.39	0.24				0.74	0.29			23 Feb Exp6
60	28.69	0.45	1.59	0.24	0.74	1.23	0.77	3.45	0.99	5 Feb Exp1
60	31.29	0.50	0.41	0.22	0.80	1.38	0.75	3.93	1.17	5 Feb Exp2
60	33.9	0.54	0.18	0.17	0.78	1.30	0.77	4.15	1.27	5 Feb Exp3
60	52.16	0.83				2.54				5 Feb Exp6
60	31.29	0.50	0.62	0.25	0.76	1.20	0.91	4.00	1.15	7 Feb Exp1
60	33.9	0.54	0.20	0.20	0.83	1.37	0.86	3.82	0.99	7 Feb Exp2
60	36.51	0.58	0.19	0.19	0.77	1.61	0.74	4.20	1.22	7 Feb Exp3
60	39.12	0.62	0.16	0.16	0.73	1.59	0.83	4.27	1.07	7 Feb Exp4
60	41.73	0.66	0.15	0.15	0.67	1.82	0.79	4.98	1.32	7 Feb Exp5
60	44.34	0.70	0.13	0.13	0.64	1.90	0.75	5.27	1.11	7 Feb Exp6
60	49.55	0.79	0.13	0.13	0.63	2.13	0.75	5.64	1.17	7 Feb Exp7
60	54.77	0.87	0.12	0.12	0.60	2.31	0.77	6.00	1.13	7 Feb Exp8
60	59.46	0.94	0.12	0.12	0.58	2.16	0.74	6.25	1.26	7 Feb Exp9

Table A3. Summary of Shallow Water Experiments (Section 4.8)

Angle	F_r	dF/H	$S_{sur}d/H$	S_td/H	x_t/H	x_i/H	S_id/H	x_n/H	S_nd/H	Exp ID
60	65.2	1.03	0.11	0.11	0.56	2.32	0.77	6.45	1.13	7 Feb Exp10
60	70.42	1.12	0.12	0.12	0.58	2.43	0.75			7 Feb Exp11
60	29.99	0.48	0.99	0.29	0.77	1.18	0.88	4.04	0.98	11 Feb Exp1
60	32.6	0.52	0.24	0.24	0.83	1.44	0.72	4.04	0.96	11 Feb Exp2
60	62.6	0.99	0.15	0.15	0.58	2.53	0.75			11 Feb Exp3
60	67.81	1.07	0.13	0.13	0.56	2.47	0.81			11 Feb Exp4
60	73.03	1.16	0.13	0.13	0.54	2.40	0.72			11 Feb Exp5
60	80.85	1.28	0.13	0.13	0.54	2.33	0.81			11 Feb Exp6